Journal of Sound and Vibration 569 (2024) 117940

Contents lists available at ScienceDirect

Journal of Sound and Vibration

journal homepage: www.elsevier.com/locate/jsvi

An alternative approach to model the dynamics of a milling tool

Kaidong Chen [a,b], He Zhang [a], Nathan van de Wouw [b], Emmanuel Detournay [a,*]

[a] Department of Civil, Environmental and Geo-Engineering, University of Minnesota, Minneapolis, MN 55455, USA
[b] Department of Mechanical Engineering, Eindhoven University of Technology, P.O. Box 513, 5600MB Eindhoven, The Netherlands

ARTICLE INFO

Keywords:
Milling
Tool/machine dynamics
Chip thickness
Modeling and numerical simulation
PDE–ODE formulation

ABSTRACT

Mathematical models play an increasing role in understanding and predicting machining processes, in particular milling. However, despite the considerable efforts that have been dedicated to this problem, a majority of milling models still rely on simplifying assumptions to calculate the chip thickness. In this paper, the chip thickness is determined without these simplifications, based on a surface function that describes the milled surface and on information about the workpiece boundary. By combining the partial differential equation (PDE) governing the evolution of this surface function with the ordinary differential equations (ODE) governing the tool/machine dynamics, a mixed PDE–ODE formulation is proposed to describe the dynamics of the milling process. The coupled system of differential equations is solved using an algorithm that combines finite difference (ODE) and finite volume (PDE) methods. A case study is presented to compare the proposed approach with the classical delay differential equations (DDE) model formulation for milling processes based on a simplified chip thickness model. The PDE–ODE formulation represents an explicit mathematical model for milling process dynamics; it yields a theoretically exact chip thickness and offers a means to assess the validity of models based on DDE formulation. Moreover, the proposed formulation is capable of simulating transient tool behaviors when the tool is milling the outer region of the workpiece, which is in general neglected by the DDE-based models.

1. Introduction

Milling is a basic manufacturing process in various fields of engineering [1], including aeronautics [2], bio-medicine [3], and automobiles [4]. Motivated by the need to mitigate chatter [5,6] – a self-excited vibration of the tool which affects the surface finish of the workpiece – research on milling dynamics began in the 1950s [7]. According to [8], the dynamic models of milling can be classified into Class I models that only consider the movement of the tool and Class II models that simulate both the tool dynamics and the evolution of the machined surface.

Class I models compute the chip thickness using the current and previous positions of the tool. Specifically, the chip thickness is divided into a static chip thickness created by the prescribed motion of the tool and a dynamic one caused by parasitic vibrations [9]. The static chip thickness is determined by assuming either a simplified circular tooth path [10,11] or a realistic trochoidal tooth path [9,12]. On the other hand, the dynamic chip thickness is computed using the current (at time t) and one or more preceding (at time $t - \Delta t_i$) positions of the tool center, where Δt_i is referred to as the time delay. A single constant time delay is used in [13,14], but other models rely on a variable time delay [9,15], or two discrete ones [16], or even multiple ones [17,18] to improve accuracy. Mathematically, all proposed Class I models are governed by a system of delay differential equations (DDE) [13,19]. Taking advantage of this explicit mathematical formulation, DDE-based models have been widely used to conduct stability analysis

* Corresponding author.
E-mail address: detou001@umn.edu (E. Detournay).

https://doi.org/10.1016/j.jsv.2023.117940
Received 4 February 2023; Received in revised form 4 July 2023; Accepted 11 July 2023
Available online 18 July 2023
0022-460X/© 2023 Elsevier Ltd. All rights reserved.

in both frequency [20,21] and time [22,23] domains, for both normal [20,24] and low radial immersion [25,26] milling processes. Furthermore, these models have been adopted to identify cutting force coefficients [27] and to predict milling accuracy [14]. However, DDE-based models can lead, in some cases, to less reliable predictions because of errors resulting from their approximated chip thickness and time delay models. Although a subclass of Class I models [28,29] allows to compute the chip thickness without relying on the usual approximations of DDE-based models, it lacks a clear and explicit mathematical formulation of the model.

On the other hand, Class II models can determine the chip thickness directly because the milled surface around the tool is fully constructed. This milled surface is updated according to the tool motion and, in turn, brings a feedback to the tool movement via its force interactions with the cutters. From this perspective, Class II models couple a representation of the milled surface with the tool dynamics model to describe the milling process.

Multiple discrete surface models have been proposed in the literature. The concept of a "surface array" is introduced in [30] , which provides a discrete description of the evolution of the milled surface around the tool. A similar concept is adopted in [31] for low radial immersion milling and in [32] to account for the effect of tool run-out. In [8], the surface is approximated by discrete points connected by straight-lines and is updated through a material removal model. For micro-milling, a surface consisting of a set of discrete surface points is introduced in [33] to describe the surface evolution, taking into account the elastic recovery after the passage of the cutter. Although the Class II models provide a straight-forward way to compute the chip thickness from the evolution of the milled surface, the published Class II models focus on the numerical discretization of the surface without the benefit of a systematic mathematical framework, unlike DDE-based Class I models.

The core contribution of this paper is formulating the mathematical underpinning of the Class II models. Theoretically, this mathematical model enables an exact determination of the chip thickness, and thus provides a means to assess the validity of DDE-based Class I models that rely on simplified chip thickness calculations. In this paper, a partial differential equation (PDE) governing the evolution of the machined surface [34][1] is combined with a system of ordinary differential equations (ODE) governing the tool dynamics. This leads to a mixed PDE–ODE formulation for Class II models. Based on this mathematical framework, an algorithm combining the finite difference method (FDM) and the finite volume method (FVM) is developed to solve the model numerically. Simulation results show that the PDE–ODE formulation agrees generally well with the DDE formulation but is more accurate when the ratio of the stiffness of the cutting interface to that of the milling system is relatively large. Besides, the proposed PDE–ODE formulation can accurately describe the transient tool behavior when the tool is milling the outer regions of the workpiece, which often cannot be accurately described in the DDE-based models.

The rest of the article is organized as follows. In Section 2, the mixed system of PDE–ODE governing the tool dynamics is formulated, and the boundary conditions and conditions at the cutters are also articulated. In Section 3, a dimensionless form of the mathematical model is derived. The algorithm to solve the PDE–ODE formulation is introduced in Section 4, and a case study is conducted in Section 5 to compare the proposed model with the conventional DDE formulation. Finally, conclusions are drawn in Section 6.

2. Mathematical model

2.1. Tool dynamics

Following [9], the dynamics of the milling tool/machine is reduced to the mass–spring–damper system illustrated in Fig. 1(a). The governing equations read

$$\begin{aligned} &M_X \ddot{X}_T + C_X(\dot{X}_T - V_0) + K_X(X_T - V_0 t) = F_X \\ &M_Y \ddot{Y}_T + C_Y \dot{Y}_T + K_Y Y_T = F_Y \,, \end{aligned} \tag{1}$$

where $X_T(t)$ and $Y_T(t)$ are the coordinates of the tool center measured in a frame (X, Y) fixed to the workpiece.[2] The prescribed movement of the tool is a uniform linear motion along the X-axis with a velocity V_0. The parameters M_I, C_I, and K_I denote the equivalent mass, damper, and stiffness in the I $(I = X, Y)$ direction. The total cutting forces in X- and Y- directions, F_X and F_Y, are the sum of the cutting force components on all the cutters

$$F_X = \sum_{i=1}^{N} F_{Xi} \,, \qquad F_Y = \sum_{i=1}^{N} F_{Yi} \,, \tag{2}$$

where N is the total number of cutters. The cutting force components for cutter i, F_{Xi} and F_{Yi}, along the X- and Y-axes are determined through a coordinate transformation from the cutter frame to the global frame (X, Y) (see Fig. 1 (b)).

$$\begin{bmatrix} F_{Xi} \\ F_{Yi} \end{bmatrix} = \begin{bmatrix} -\cos\phi_i(t) & -\sin\phi_i(t) \\ \sin\phi_i(t) & -\cos\phi_i(t) \end{bmatrix} \begin{bmatrix} F_{ti} \\ F_{ri} \end{bmatrix} \,, \tag{3}$$

where $\phi_i(t) = \theta_i + \Omega t + \Theta_0$ is the instantaneous angle between the Y -axis and the cutter i. Here θ_i is the orientation of the cutter measured in the tool frame (x, y), Ω is the constant spindle speed of the tool and Θ_0 is the initial angular difference between the

[1] The research in [34] is partly inspired from [35,36], where a partial differential equation (PDE) formulation has been developed to describe the evolution of the machined surface in the turning process.

[2] For the sake of simplicity, we focus on the second-order tool/machine dynamics in X- and Y- directions in (1). However, the model can readily be extended to include high-order (multi-modal) tool/machine dynamics.

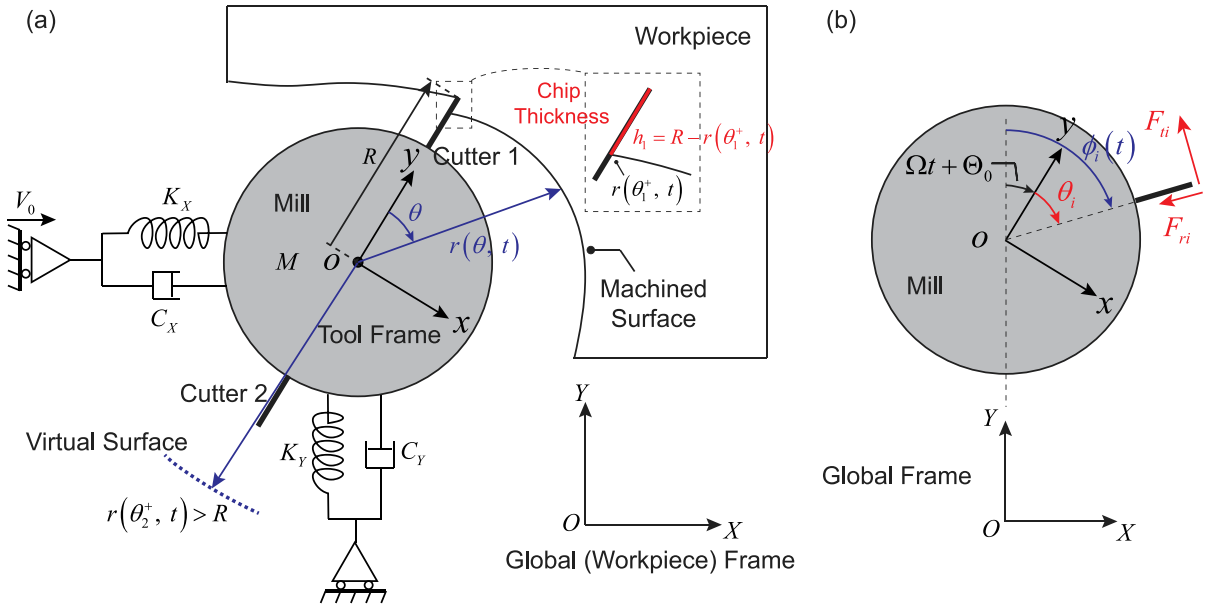

Fig. 1. (a) The mass–spring–damper model of the milling tool/machine dynamics. (b) Coordinate transformation of the cutting force at the cutter.

(x, y) and (X, Y) frames. Without loss of generality, the y-axis of the (x, y) frame is aligned with an arbitrary cutter of the tool. This cutter is numbered as Cutter 1 and the other cutters are sequentially numbered clockwise, see Fig. 1 (a). This numbering order of the cutters is used throughout the paper.

The tangential and radial cutting force components on the cutter i, F_{ti} and F_{ri} in (3), can be described by the so-called exponential model [9,37]:

$$F_{ti} = K_t a_p h_i^{\beta}(t)\,, \qquad F_{ri} = K_r a_p h_i^{\beta}(t)\,, \qquad i = 1, 2, \ldots, N\,, \tag{4}$$

where K_t, K_r, and $0 \le \beta \le 1$ are cutting parameters, a_p is the axial depth of cut and h_i denotes the chip thickness faced by cutter i.

2.2. Surface function

Determination of the cutting force based on (4) requires an accurate computation of the chip thickness. This can be achieved using the concept of surface function introduced in [34]. As shown in Fig. 1(a), the distance between the tool center and the milled surface can be viewed as a function of orientation θ and time t: $r(\theta, t)$, which is defined as the surface function. Physically, this surface function describes the geometry of the machined surface viewed from the moving tool center; it is thus updated according to the movement of the tool center, see Section 2.2.1. From the known surface function, the chip thickness is readily computed through

$$h_i = \max\left\{0,\ R - r\left(\theta_i^+, t\right)\right\}\,, \qquad i = 1, 2, \ldots, N\,, \tag{5}$$

where R is the radius of the tool from tool center to tip of the cutter, and $r\left(\theta_i^+, t\right)$ represents the distance between the tool center and the surface just ahead of cutter i (at orientation θ_i). For example, Cutter 1 in Fig. 1(a) is removing material from the workpiece. Mathematically, this is described by $R > r\left(\theta_1^+, t\right)$, where $\theta_1 = 0$ is the orientation of Cutter 1 measured in the tool frame (x, y). The chip thickness at Cutter 1 is then given by $h_1 = R - r\left(\theta_1^+, t\right)$. As for Cutter 2 at the orientation θ_2, there is no material removal in the scenario in Fig. 1(a) and thus the chip thickness is zero. The concept of virtual surface [34] is introduced to account for the absence of material to be machined by setting $r\left(\theta_2^+, t\right) > R$.[3] According to (5), the chip thickness in this case is $h_2 = 0$, reflecting that there is no contact interaction between the workpiece and the cutter.

The surface function enables the detection of the loss of contact between an arbitrary cutter i and the workpiece, by comparing $r\left(\theta_i^+, t\right)$ and R. The cutter loses contact with the workpiece when $r\left(\theta_1^+, t\right) > R$, and the chip thickness h_i on the cutter is consequently set to zero through (5), thus causing the cutting forces on the cutter also drop to zero according to (4). This model aspect is later verified through a case study in Section 5.2.

[3] Strictly following the definition of the surface function, it should be defined as $r(\theta_i, t) = +\infty$ if there is no material at orientation θ_i. In order to avoid the mathematical and numerical difficulties caused by positive infinity, a number sufficient larger than R is artificially defined instead, which can be viewed as a virtual surface $r(\theta_i, t) > R$.

2.2.1. Evolution of the surface function

According to [34], the evolution of the surface function around the tool is governed by a PDE in the form of a conservation law:

$$\frac{\partial r}{\partial t} + \frac{\partial f}{\partial \theta} = \psi \,, \tag{6}$$

where

$$f\,(r,\,\theta,\,t) = -\Omega r - V_t \ln r \,, \quad \psi\,(r,\,\theta,\,t) = V_r\,(\ln r - 1) \tag{7}$$

with

$$V_t = V\cos\left(\theta + \Omega t + \Theta_0 + \Phi\right) \,, \quad V_r = V\sin\left(\theta + \Omega t + \Theta_0 + \Phi\right) \,. \tag{8}$$

In the above equation, V is the magnitude of velocity of the tool center and Φ is the inclination of the velocity with respect to the X-axis of the global frame $(X,\,Y)$

$$V = \sqrt{\dot{X}_T^2 + \dot{Y}_T^2} \,, \qquad \tan\Phi = \dot{Y}_T / \dot{X}_T \,, \tag{9}$$

Here the condition, stated in [34], that the $(x,\,y)$ and $(X,\,Y)$ frames initially coincide, is relaxed; as a result, the term Ωt in the original PDE derived in [34] is replaced by $\Omega t + \Theta_0$.

Physically, function f is associated with the relative rotation of the tool with respect to the workpiece, while function ψ is related to the relative radial movement of the tool with respect to the workpiece. These relative movements govern the evolution of the surface function, see Appendix A for more detailed explanations.

2.2.2. Conditions at cutters

Consider an arbitrary cutter i at orientation θ_i, and let $r\left(\theta_i^-,\,t\right)$ and $r\left(\theta_i^+,\,t\right)$ represent the instantaneous distances between the tool center and the machined surface just behind and in front of the cutter, respectively. Since Cutter 1 is removing material and creating a new surface (see Fig. 1(a)), the discontinuous condition

$$r\left(\theta_1^-,\,t\right) = R > r\left(\theta_1^+,\,t\right) \,, \tag{10}$$

at θ_1 reflects that the cutter is creating a new machined surface. In contrast, Cutter 2 is not in contact with the workpiece: $r\left(\theta_2^+,\,t\right) > R$, thus the surface function is continuous at θ_2:

$$r\left(\theta_2^-,\,t\right) = r\left(\theta_2^+,\,t\right) \,. \tag{11}$$

In summary, the conditions accounting for possible material removal process at the cutters are

$$r\left(\theta_i^-,\,t\right) = \max\left\{r\left(\theta_i^+,t\right),\,R\right\} \,, \qquad i = 1,\,2\,,\ldots,\,N \,. \tag{12}$$

2.2.3. Boundary condition of the PDE

By introducing a virtual surface, the surface function is defined for $\theta \in [0,\,2\pi]$. Given that $\theta = 0$ and $\theta = 2\pi$ refer to the same direction, the following periodic boundary condition holds

$$r\,(2\pi,\,t) = r\,(0,\,t) \,. \tag{13}$$

In particular, when a cutter is exactly positioned at $\theta = 0/\theta = 2\pi$, the possibility of material removal is considered and the boundary condition becomes

$$r\,(2\pi,\,t) = \max\left\{r\,(0\,,t)\,,\,R\right\} \,. \tag{14}$$

2.2.4. Initial boundary of the workpiece

Until now, it has been assumed that the tool is fully immersed into the workpiece, see Fig. 2(a). However, the *initial* boundary of the workpiece, abbreviated as IBW in below, can also affect the chip thickness computation when the cutter is close to the outer edge of the workpiece, see Fig. 2(b). Accordingly, the chip thickness model in (5) needs to be modified, which is discussed in below.

To begin with, the following assumptions are made:

1. The *initial* shape of the workpiece is known, i.e., the information of the IBW is known.
2. The *initial* shape of the workpiece is convex, and the IBW is continuous and closed.
3. The cutter can intersect with at most two points of the IBW.

Similarly to the surface function for the milled surface, the IBW can be described by an IBW function $\widetilde{r}(\theta,\,t)$, see Fig. 3. Depending on whether the tool center is inside the IBW or not, the IBW function can be either single-valued or double-valued. As we have assumed, mathematically the *initial* shape of the workpiece can be viewed as a convex set C_w in the global $(X,\,Y)$ frame (see Fig. 3(a)), which is used to distinguish the single-valued case in Fig. 3(b) and the double-valued one in Fig. 3(c). The distance from the tool center $\mathbf{Z}_T = \left(X_T,\,Y_T\right)$ to the convex set C_w is defined as

$$\mathrm{dist}_{C_w}\left(\mathbf{Z}_T\right) = \left\|\mathbf{Z}_T - \mathrm{prox}_{C_w}\left(\mathbf{Z}_T\right)\right\| \,, \tag{15}$$

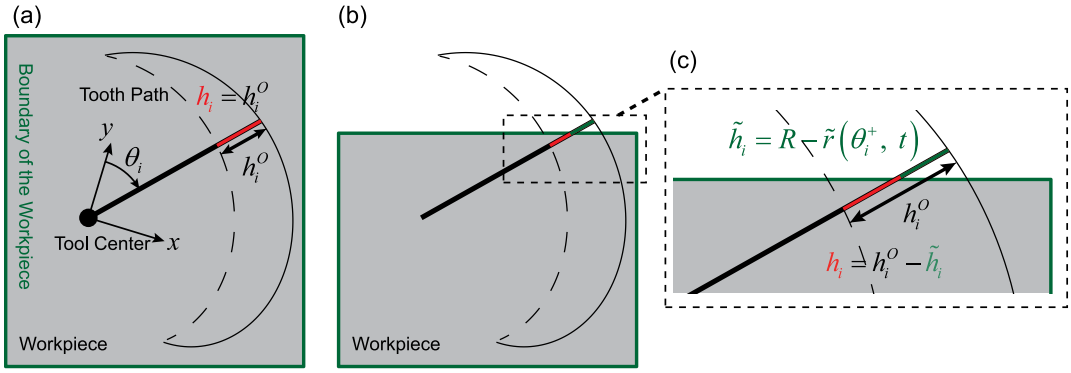

Fig. 2. The influence of the workpiece boundary on the chip thickness when the tool center is inside the IBW: (a) the cutter does not reach the boundary; (b) the cutter reaches the boundary. (c) Zoomed cutting details of figure (b).

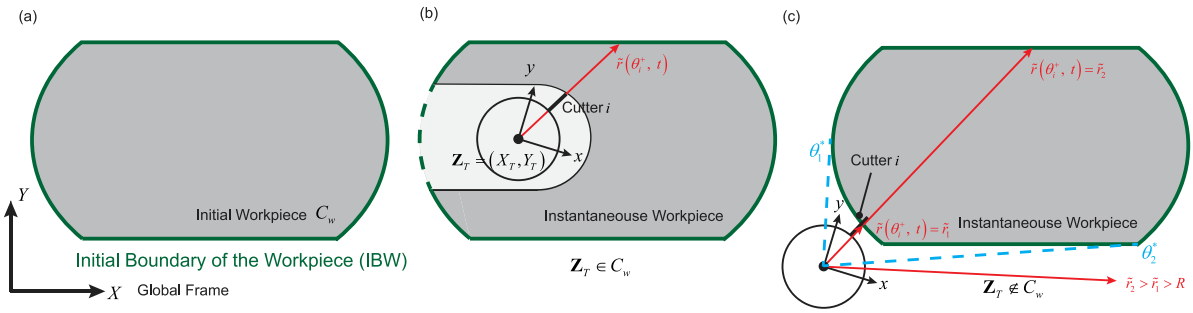

Fig. 3. IBW function, describing (a) the initial boundary of the workpiece (IBW), measured from the tool center: (b) single-valued case and (c) double-valued case.

with

$$\mathrm{prox}_{C_w}(\mathbf{Z}_T) = \underset{\mathbf{X}\in C_w}{\mathrm{argmin}} \|\mathbf{Z}_T - \mathbf{X}\| := \left\{\mathbf{X}^* \in C_w : \|\mathbf{Z}_T - \mathbf{X}^*\| \le \|\mathbf{Z}_T - \mathbf{X}\| \text{ for all } \mathbf{X} \in C_w\right\} . \tag{16}$$

Mathematically, $\mathbf{Z}_T \in C_w$ when $\mathrm{dist}_{C_w}(\mathbf{Z}_T) = 0$ [38]; physically this reflects that the tool center is inside the IBW and the IBW function $\tilde{r}(\theta, t)$ is single-valued, see Fig. 3(b). In contrast, $\mathbf{Z}_T \notin C_w$ when $\mathrm{dist}_{C_w}(\mathbf{Z}_T) > 0$, reflecting that the tool center is outside the IBW and the IBW function $\tilde{r}(\theta, t)$ is double-valued, see Fig. 3(c). The case when the tool center is exactly on the IBW is not considered here. Given that the initial shape of the workpiece is assumed known, we only need to determine the position of the tool center in the global frame and then $\tilde{r}(\theta, t)$ is readily determined for both single-valued and double-valued cases. When the tool center is outside the IBW, the IBW function $\tilde{r}(\theta, t)$ is defined only in a range of orientations around the tool center ($\theta \in [\theta_1^*, \theta_2^*]$), see Fig. 3(c). For orientations where there is no workpiece, $\tilde{r}(\theta, t)$ is artificially set to large enough values $\tilde{r}_2 > \tilde{r}_1 > R$ to ensure that the computation of the chip thickness is not influenced by $\tilde{r}(\theta, t)$ for $\theta \notin [\theta_1^*, \theta_2^*]$.

When the IBW function is single-valued (see Fig. 3(b)), we can directly determine whether or not the cutter has reached the IBW by comparing the tool radius R and the boundary information just ahead of the cutter $\tilde{r}(\theta_i^+, t)$. If the cutter does not reach the IBW ($R < \tilde{r}(\theta_i^+, t)$), (5) holds. In contrast, if the cutter reaches this boundary ($R > \tilde{r}(\theta_i^+, t)$), computation of the chip thickness in (5) needs to be modified. When the IBW function is double-valued (see Fig. 3(c)), the two values $\tilde{r}_1$ and $\tilde{r}_2$ ($\tilde{r}_1 < \tilde{r}_2$) both need to be compared with R to determine the possible intersection(s) between the cutter and the IBW. The cutter does not reach the IBW when $R < \tilde{r}_1$; the cutter intersects with the IBW at one single point when $\tilde{r}_1 < R < \tilde{r}_2$; the cutter intersects with the IBW at two different points when $R > \tilde{r}_2$.

Fig. 2(a–c) illustrates the modified chip thickness model when the tool center is inside the initial workpiece boundary ($\mathrm{dist}_{C_w}(\mathbf{Z}_T) = 0$). When the cutter does not reach the initial workpiece boundary ($R < \tilde{r}(\theta_i^+, t)$) , the original chip thickness h_i^O computed by (5) is still the correct chip thickness, see Fig. 2(a). In contrast, an extra subtraction of $\tilde{h}_i = R - \tilde{r}(\theta_i^+, t)$ to h_i^O is required when the cutter reaches the boundary ($R > \tilde{r}(\theta_i^+, t)$), see Fig. 2(b–c). The modified chip thickness model for these two cases can be summarized as

$$h_i = \max\left\{0,\ h_i^O - \tilde{h}_i\right\} , \qquad \text{when } \mathrm{dist}_{C_w}(\mathbf{Z}_T) = 0 \tag{17}$$

with

$$h_i^O = \max\left\{0,\ R - r(\theta_i^+, t)\right\} , \qquad \tilde{h}_i = \max\left\{0,\ R - \tilde{r}(\theta_i^+, t)\right\} , \qquad i = 1, 2, \ldots, N . \tag{18}$$

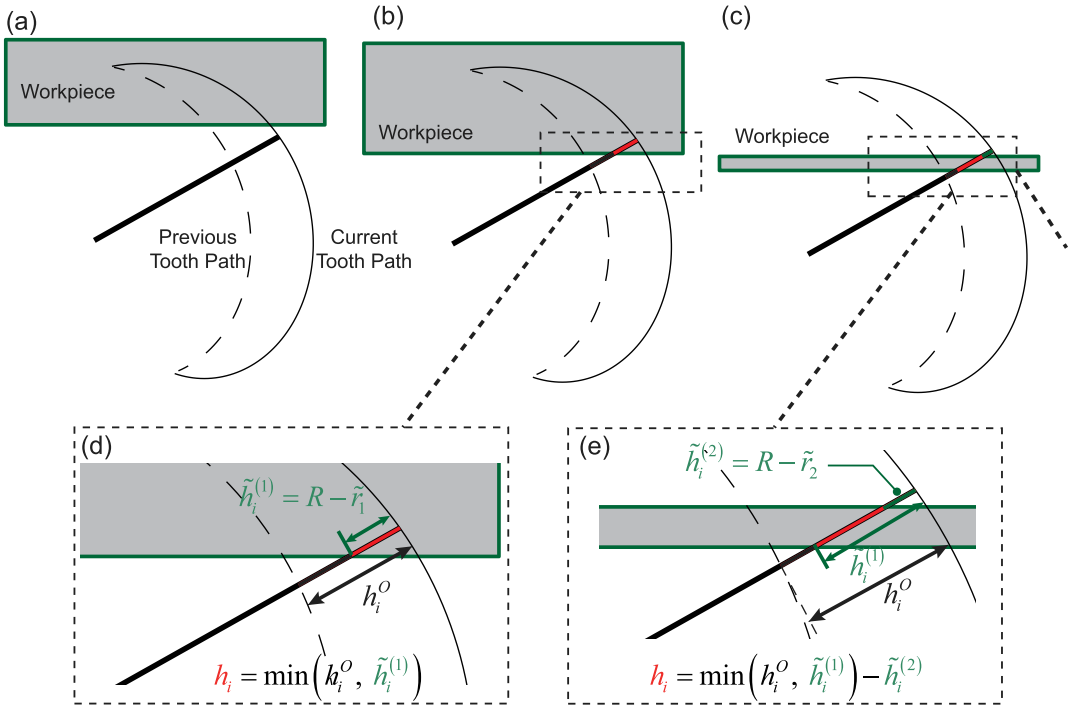

Fig. 4. The influence of the workpiece boundary on the chip thickness when the tool center is outside the IBW: (a) the cutter does not reach the boundary; (b) the cutter intersects with the IBW at one single point; (c) the cutter intersects with the IBW at two different points. (d–e) Zoomed cutting details of figure (b–c), respectively.

It is noted that (17) degenerates to (5) when $R < \tilde{r}\left(\theta_i^+, t\right)$, reflecting that the initial boundary of the workpiece does not influence the chip thickness ahead of the cutter when the cutter does not reach the boundary.

Fig. 4(a–e) illustrates the modified chip thickness model when the tool center is outside the IBW ($\mathrm{dist}_{C_w}\left(\mathbf{Z}_T\right) > 0$). As illustrated in Fig. 4(a), the chip thickness is zero when the cutter does not reach the boundary ($R < \tilde{r}_1$). When the cutter intersects with the IBW at one single point ($\tilde{r}_1 < R < \tilde{r}_2$), the realistic chip thickness is the minimum value between h_i^O and $\tilde{h}_i^{(1)} = R - \tilde{r}_1$, see Fig. 4(b) and (d). When the cutter intersects with the IBW at two different points ($R > \tilde{r}_2$, see Fig. 4(c) and (e)), an extra subtraction of $\tilde{h}_i^{(2)} = R - \tilde{r}_2$ is required. In summary, the modified chip thickness model when the tool center is outside the IBW is:

$$h_i = \max\left\{0,\ \min\left\{h_i^O, \tilde{h}_i^{(1)}\right\} - \tilde{h}_i^{(2)}\right\}, \qquad \text{when } \mathrm{dist}_{C_w}\left(\mathbf{Z}_T\right) > 0 \tag{19}$$

with

$$\tilde{h}_i^{(1)} = \max\left\{0,\ R - \tilde{r}_1(i)\right\}, \qquad \tilde{h}_i^{(2)} = \max\left\{0,\ R - \tilde{r}_2(i)\right\}, \qquad i = 1, 2, \ldots, N, \tag{20}$$

where $\tilde{r}_1(i)$ and $\tilde{r}_2(i)$ denote the two values of the IBW function just ahead of cutter i. In summary, the comprehensive expression for the chip thickness is

$$h_i = \begin{cases} \max\left\{0,\ h_i^O - \tilde{h}_i\right\}, & \mathrm{dist}_{C_w}\left(\mathbf{Z}_T\right) = 0 \\ \max\left\{0,\ \min\left\{h_i^O, \tilde{h}_i^{(1)}\right\} - \tilde{h}_i^{(2)}\right\}, & \mathrm{dist}_{C_w}\left(\mathbf{Z}_T\right) > 0, \end{cases} \qquad i = 1, 2, \ldots, N. \tag{21}$$

Eq. (21) is an exact expression for computing the chip thickness, unlike the simplified chip thickness models used in the DDE formulation.

2.3. Mixed PDE-ODE formulation for the milling process dynamics

In Sections 2.1 and 2.2, we have respectively introduced the system of ODEs governing the movement of the tool and the PDE describing the evolution of the milled surface around the tool. These two systems are coupled via the tool center velocity and the cutting force. On the one hand, the magnitude and the direction of the tool center velocity (governed by the ODE system) are the controlling parameters in the PDE system. On the other hand, the surface function (determined by the PDE system) directly affects the chip thickness and thus the cutting force, which serves as an input to the ODE system. Therefore, a mixed PDE–ODE formulation has been established to describe the milling dynamics (see Fig. 5).

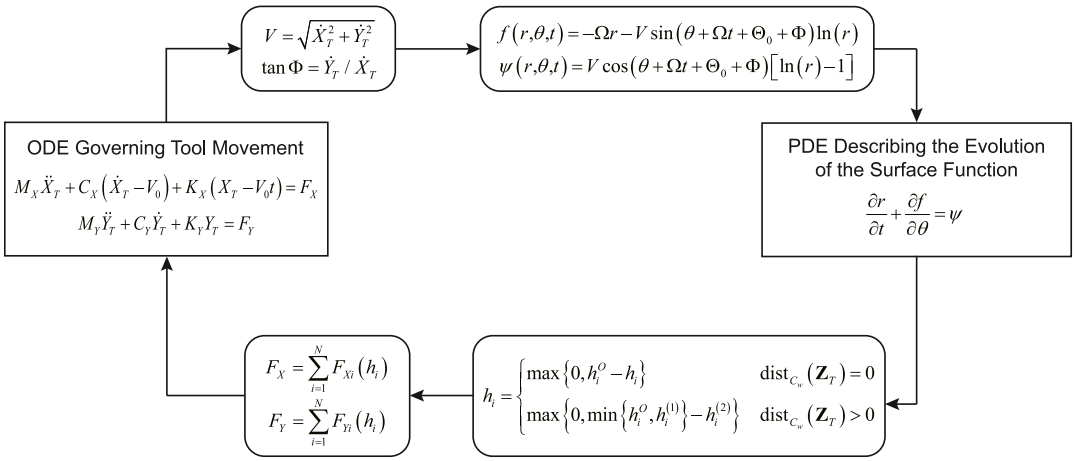

Fig. 5. The mixed PDE–ODE formulation describing the milling dynamics.

3. Scaling

In order to identify the key parameters of the system, a scaling analysis is conducted in this section.

3.1. Scaled parameters

Now we introduce a time scale t_*, a length scale ℓ_*, and a force scale F_* to rewrite the PDE–ODE system in a dimensionless form

$$t_*=\sqrt{\frac{M_X}{K_X}},\qquad \ell_*=f_z,\qquad F_*=K_ta_p\ell_*^{\beta},\tag{22}$$

where $2\pi t_*$ is the period of the resonant vibration of the discrete milling system in X-direction, $\ell_*=f_z=\frac{2\pi V_0}{N\Omega}$ is the feed per tooth [9], and F_* is the tangential component of the cutting force when the chip thickness is $\ell_*=f_z$, the maximum chip thickness when the tool moves rigidly under the prescribed motion without vibrations [9,34].

The scaled tool center coordinates then become

$$\mathcal{X}=\frac{(X_T-V_0t)}{\ell_*},\qquad \mathcal{Y}=\frac{Y_T}{\ell_*},\tag{23}$$

where V_0t is the prescribed motion of the tool. Therefore, $\mathcal{X}$ describes the perturbation along the X-axis with respect to the prescribed movement of the tool. The dimensionless surface function, IBW function, tool radius, chip thickness, and the dimensionless depth of cut are respectively defined as

$$\rho(\theta,\tau)=\frac{r(\theta,t)}{\ell_*},\qquad \tilde{\rho}(\theta,\tau)=\frac{\tilde{r}(\theta,t)}{\ell_*},\qquad \mathcal{R}=\frac{R}{\ell_*},\qquad \eta_i=\frac{h_i}{\ell_*},\quad i=1,2,\ldots,N.\tag{24}$$

where $\tau=t/t_*$ is the scaled time.

The scaled forces on the ith cutter are defined as

$$\mathcal{F}_{ti}=\frac{F_{ti}}{F_*}=\eta_i^{\beta},\qquad \mathcal{F}_{ri}=\frac{F_{ri}}{F_*}=\xi\eta_i^{\beta},\tag{25}$$

where $\xi=K_r/K_t$ is the ratio of the cutting force coefficients. Moreover, the scaled lumped parameters describing the characteristics of the milling rig are

$$\zeta_{\mathcal{X}}=\frac{C_X\Omega}{K_X},\qquad \gamma_M=\frac{M_X}{M_Y},\qquad \gamma_C=\frac{C_X}{C_Y},\qquad \gamma_K=\frac{K_X}{K_Y},\tag{26}$$

where $\zeta_{\mathcal{X}}$ is the scaled damping factor in X-direction and γ_M, γ_C, γ_K are respectively the ratios of mass, damper, and stiffness in X- and Y-directions.

Finally, two dimensionless control parameters are introduced

$$\omega=\Omega\sqrt{\frac{M_X}{K_X}},\qquad \mathcal{P}=\frac{K_ta_p\ell_*^{\beta-1}}{K_X},\tag{27}$$

where ω is the scaled spindle speed and $\mathcal{P}$ is the scaled axial depth of cut. From another perspective, ω can be viewed as the ratio of two time scales $\omega = t_*/t_0$, where $t_0 = 1/\Omega$ is the time when the mill rotates by 1 rad. Similarly, $\mathcal{P}$ can also be viewed as the ratio of two length scales $\mathcal{P} = \ell_X/\ell_*$. Here ℓ_X is the static tool center displacement in the X-direction under the force scale F_*:

$$K_X \ell_X = F_* = K_t a_p \ell_*^{\beta} \Rightarrow \mathcal{P} = \frac{\ell_X}{\ell_*} = \frac{K_t a_p \ell_*^{\beta-1}}{K_X} . \tag{28}$$

According to (28), $\mathcal{P}$ reflects the ratio of the stiffness of the cutting interface to the stiffness of the milling rig. The typical range of ω is $0 \sim 1$ [9,39] and that of $\mathcal{P}$ is $0 \sim 4$ [9,37].

3.2. Scaled mathematical models

Using the scales ℓ_*, t_*, and F_*, the ODE governing the tool dynamics can be rewritten in a dimensionless form as

$$\begin{aligned} &\ddot{\mathcal{X}} + \zeta_{\mathcal{X}} \dot{\mathcal{X}} + \mathcal{X} = \mathcal{F}_{\mathcal{X}} \\ &\gamma_M \ddot{\mathcal{Y}} + \gamma_C \zeta_{\mathcal{X}} \dot{\mathcal{Y}} + \gamma_K \mathcal{Y} = \mathcal{F}_{\mathcal{Y}} . \end{aligned} \tag{29}$$

The PDE describing the evolution of the surface around the tool becomes

$$\frac{\partial \rho}{\partial \tau} + \frac{\partial \bar{f}}{\partial \theta} = \bar{\psi} , \tag{30}$$

with

$$\begin{aligned} &\bar{f}(\rho, \theta, \tau) = -\omega\rho - \mathcal{V} \cos\left(\theta + \omega\tau + \Theta_0 + \Phi\right) \ln \rho \\ &\bar{\psi}(\rho, \theta, \tau) = \mathcal{V} \sin\left(\theta + \omega\tau + \Theta_0 + \Phi\right) (\ln \rho - 1) . \end{aligned} \tag{31}$$

The dimensionless boundary condition of the PDE is

$$\rho(2\pi, \tau) = \begin{cases} \max\{\rho(0, \tau), \mathcal{R}\} , & \text{when there is a cutter at } \theta = 0 \\ \rho(0, \tau) , & \text{otherwise} . \end{cases} , \tag{32}$$

The material removal process at the cutters can be described by

$$\rho\left(\theta_i^-, \tau\right) = \max\left\{\rho\left(\theta_i^+, \tau\right), \mathcal{R}\right\} , \qquad i = 1, 2, \ldots, N . \tag{33}$$

It is noted that the tool is first assumed to be 100% immersed while updating the PDE; then the modification considering the IBW is introduced in the computation of the chip thickness (see (36) below).

The ODE in (29) and the PDE in (30) and (31) are coupled via the tool center velocity $\{\mathcal{V}, \Phi\}$ and the cutting forces $\left\{\mathcal{F}_{\mathcal{X}}, \mathcal{F}_{\mathcal{Y}}\right\}$ given by

$$\mathcal{V} = \sqrt{\left(\dot{\mathcal{X}} + \frac{\omega N}{2\pi}\right)^2 + \dot{\mathcal{Y}}^2} , \qquad \tan\Phi = \dot{\mathcal{Y}} / \left(\dot{\mathcal{X}} + \frac{\omega N}{2\pi}\right) . \tag{34}$$

$$\begin{bmatrix} \mathcal{F}_{\mathcal{X}} \\ \mathcal{F}_{\mathcal{Y}} \end{bmatrix} = \sum_{i=1}^{N} \begin{bmatrix} -\cos\phi_i(\tau) & -\sin\phi_i(\tau) \\ \sin\phi_i(\tau) & -\cos\phi_i(\tau) \end{bmatrix} \begin{bmatrix} 1 \\ \xi \end{bmatrix} \mathcal{P} \eta_i^{\beta} \tag{35}$$

with $\phi_i(\tau) = \theta_i + \omega\tau + \Theta_0$ and

$$\eta_i = \begin{cases} \max\left\{0, \eta_i^O - \tilde{\eta}_i\right\} , & \mathrm{dist}_{\overline{C}_w}\left(\overline{\mathbf{Z}}_T\right) = 0 \\ \max\left\{0, \min\left\{\eta_i^O, \tilde{\eta}_i^{(1)}\right\} - \tilde{\eta}_i^{(2)}\right\} , & \mathrm{dist}_{\overline{C}_w}\left(\overline{\mathbf{Z}}_T\right) > 0 , \end{cases} \qquad i = 1, 2, \ldots, N , \tag{36}$$

where

$$\eta_i^O = \max\left\{0, \mathcal{R} - \rho\left(\theta_i^+, t\right)\right\} , \qquad i = 1, 2, \ldots, N . \tag{37}$$

When $\mathrm{dist}_{\overline{C}_w}\left(\overline{\mathbf{Z}}_T\right) = 0$,

$$\tilde{\eta}_i = \max\left\{0, \mathcal{R} - \tilde{\rho}\left(\theta_i^+, t\right)\right\} , \qquad i = 1, 2, \ldots, N , \tag{38}$$

and when $\mathrm{dist}_{\overline{C}_w}\left(\overline{\mathbf{Z}}_T\right) > 0$,

$$\tilde{\eta}_i^{(1)} = \max\left\{0, \mathcal{R} - \tilde{\rho}_1(i)\right\} , \qquad \tilde{\eta}_i^{(2)} = \max\left\{0, \mathcal{R} - \tilde{\rho}_2(i)\right\} , \qquad i = 1, 2, \ldots, N \tag{39}$$

with $\tilde{\rho}_1(i) = \tilde{r}_1(i)/\ell_*$ and $\tilde{\rho}_2(i) = \tilde{r}_2(i)/\ell_*$. Here $\overline{C}_w$ denotes the scaled convex set describing the initial shape of the workpiece and $\overline{\mathbf{Z}}_T = \left(\mathcal{X} + \frac{\omega N}{2\pi}\tau, \mathcal{Y}\right)$.

4. Numerical algorithm for the mixed PDE-ODE model

4.1. Finite difference method for the ODE

In order to solve the ODE system (29) numerically, the motion of the tool center is discretized in time with the coordinates of the tool center denoted as $\mathbf{X}_n = [\mathcal{X}_n, \mathcal{Y}_n]^{\mathrm{T}}$ at each time step τ_n. Using the central difference method [40], coordinates $\mathbf{X}_{n+1}$ at time τ_{n+1} are calculated using the known coordinates $\mathbf{X}_n$ and $\mathbf{X}_{n-1}$ at time τ_n and τ_{n-1}, respectively.

$$\mathbf{X}_{n+1} = \mathbf{C}_0^{-1}\left(\mathbf{F}_n - \mathbf{C}_1\mathbf{X}_n - \mathbf{C}_2\mathbf{X}_{n-1}\right), \tag{40}$$

where $\mathbf{F}_n$ is the total cutting force at time step τ_n, which will be introduced later in Section 4.3, see (50). Matrices $\mathbf{C}_0$, $\mathbf{C}_1$, and $\mathbf{C}_2$ are determined through

$$\mathbf{C}_0 = \frac{1}{\Delta\tau^2}\mathbf{M} + \frac{1}{2\Delta\tau}\mathbf{C}, \quad \mathbf{C}_1 = \mathbf{I} - \frac{2}{\Delta\tau^2}\mathbf{M}, \quad \mathbf{C}_2 = \frac{1}{\Delta\tau^2}\mathbf{M} - \frac{1}{2\Delta\tau}\mathbf{C}, \tag{41}$$

where $\Delta\tau = \tau_{n+1} - \tau_n$ is the time step and

$$\mathbf{M} = \begin{bmatrix} 1 & 0 \\ 0 & \gamma_M \end{bmatrix}, \quad \mathbf{C} = \begin{bmatrix} \zeta_{\mathcal{X}} & 0 \\ 0 & \gamma_C\zeta_{\mathcal{X}} \end{bmatrix}, \quad \mathbf{I} = \begin{bmatrix} 1 & 0 \\ 0 & \gamma_K \end{bmatrix}. \tag{42}$$

A special starting procedure should be used while computing $\mathbf{X}_1$, given the known initial conditions $\mathbf{X}_0$ and $\dot{\mathbf{X}}_0$. According to (40), we still need to determine $\mathbf{X}_{-1}$ in order to compute $\mathbf{X}_1$. To begin with, $\ddot{\mathbf{X}}_0$ can be calculated through (29) with known $\mathbf{X}_0$ and $\dot{\mathbf{X}}_0$. Then the tool center coordinate $\mathbf{X}_{-1}$ are obtained through [40]

$$\mathbf{X}_{-1} = \mathbf{X}_0 - \Delta\tau\dot{\mathbf{X}}_0 + \frac{\Delta\tau^2}{2}\ddot{\mathbf{X}}_0. \tag{43}$$

The central difference method is conditionally stable and the stability condition on the time step is given by [40]

$$\Delta\tau \le \min\left\{\sqrt{4+\zeta_{\mathcal{X}}^2} - \zeta_{\mathcal{X}}, \sqrt{\frac{\gamma_M}{\gamma_K}}\left(\sqrt{4+\left(\gamma_C\zeta_{\mathcal{X}}\right)^2} - \gamma_C\zeta_{\mathcal{X}}\right)\right\}. \tag{44}$$

4.2. Finite volume method for the PDE

Following the finite volume method introduced in [34], the machined surface around the tool is discretized into $K = M \times N$ cells. Here M is the number of cells between two neighboring cutters and it is assumed that the N cutters are uniformly distributed around the axis of revolution. The range of the kth cell C_k ($k = 1, 2, \ldots, K$) is $C_k = ((k-1)\Delta\theta, k\Delta\theta)$, where $\Delta\theta = 2\pi/K$ is the constant angular interval of each cell. As mentioned earlier, the y-axis ($\theta = 0$) is aligned along one of the cutters; this cutter is numbered as the first cutter (cutter 1) and the other cutters are sequentially numbered clockwise. Following this procedure, the cutter i is always at the boundary between cell $C_{(i-1)M}$ and $C_{(i-1)M+1}$ ($i = 1, 2, \ldots, N$). When $i = 1$, the cell C_0 is defined as the last cell C_K. The average surface function ρ_k^n is used to approximate the milled surface around the tool at each time step τ_n

$$\rho_k^n = \frac{1}{\Delta\theta}\int_{(k-1)\Delta\theta}^{k\Delta\theta} \rho\left(\theta, \tau_n\right)\,\mathrm{d}\theta, \qquad k = 1, 2, \ldots, K, \tag{45}$$

which is updated following an upwind scheme [34,41] to describe the evolution of the machined surface.

$$\rho_k^{n+1} = \rho_k^n - \frac{\Delta\tau}{\Delta\theta}\left(\bar{f}_{k+1/2}^n - \bar{f}_{k-1/2}^n - \Delta\theta\bar{\psi}_k^n\right), \tag{46}$$

with

$$\bar{f}_{k+1/2}^n = \begin{cases} \bar{f}\left(\max\left\{\rho_{k+1}^n, \mathcal{R}\right\}, \theta_{k+1}, \tau_n\right), & \text{when } k = iM,\ i = 1, 2, \ldots, N \\ \bar{f}\left(\rho_{k+1}^n, \bar{\theta}_{k+1}, \tau_n\right), & \text{otherwise}. \end{cases} \tag{47}$$

$$\bar{f}_{k-1/2}^n = \bar{f}\left(\rho_k^n, \bar{\theta}_k, \tau_n\right), \qquad \bar{\psi}_k^n = \bar{\psi}\left(\rho_k^n, \bar{\theta}_k, \tau_n\right), \tag{48}$$

where $\bar{\theta}_{k+1} = (k+1/2)\Delta\theta$, $\bar{\theta}_k = (k-1/2)\Delta\theta$, and $\bar{f}$ and $\bar{\psi}$ are defined latter in (55). The material removal process is accounted for in (47) for cells C_k with $k = iM$, $i = 1, 2, \ldots, N$.

The following CFL condition is required to ensure the convergence of the scheme [42]:

$$\mathrm{CFL} = \max\left\{|\bar{s}|\right\}\frac{\Delta\tau}{\Delta\theta} \le 1, \tag{49}$$

where $\bar{s} = -\omega - \frac{\mathcal{V}}{\rho}\cos\left(\theta + \omega\tau + \Theta_0 + \Phi\right)$. The number of cells K should be large enough to accurately describe the surface function; K subsequently determines $\Delta\theta$. Then the suitable time step is selected to satisfy both (44) and (49).

Finally, the last cell C_K is updated by taking advantage of the periodic nature of the surface function. A ghost cell C_{K+1} is set behind C_K with $\rho_{K+1}^n = \rho_1^n$ at the beginning of each time step, then ρ_K^{n+1} is readily computed through (46).

4.3. Combined FDM-FVM algorithm

As mentioned in Section 2.3, the ODE and PDE systems are coupled via the cutting force and the tool center velocity. This coupling is reflected in the FDM and FVM algorithms used to solve the PDE–ODE system. While updating the tool center coordinate through FDM in (40), the term $\mathbf{F}_n = \left[\mathcal{F}_{\mathcal{X}_n}, \mathcal{F}_{\mathcal{Y}_n}\right]^{\mathrm{T}}$ is calculated using the surface function ρ_k^n at time τ_n as follows:

$$\begin{bmatrix} \mathcal{F}_{\mathcal{X}_n} \\ \mathcal{F}_{\mathcal{Y}_n} \end{bmatrix} = \sum_{i=1}^{N} \begin{bmatrix} -\cos\phi_i\left(\tau_n\right) & -\sin\phi_i\left(\tau_n\right) \\ \sin\phi_i\left(\tau_n\right) & -\cos\phi_i\left(\tau_n\right) \end{bmatrix} \begin{bmatrix} 1 \\ \xi \end{bmatrix} \mathcal{P}\eta_{i_n}^{\beta} . \tag{50}$$

with $\phi_i\left(\tau_n\right) = \theta_i + \omega\tau_n + \Theta_0$ and

$$\eta_{i_n} = \begin{cases} \max\left\{0,\ \eta_{i_n}^{O} - \widetilde{\eta}_{i_n}\right\}, & \mathrm{dist}_{\overline{C}_w}\left(\overline{\mathbf{Z}}_T^n\right) = 0 \\ \max\left\{0,\ \min\left\{\eta_{i_n}^{O}, \widetilde{\eta}_{i_n}^{(1)}\right\} - \widetilde{\eta}_{i_n}^{(2)}\right\}, & \mathrm{dist}_{\overline{C}_w}\left(\overline{\mathbf{Z}}_T^n\right) > 0, \end{cases} \qquad i = 1, 2, \ldots, N, \tag{51}$$

where

$$\eta_{i_n}^{O} = \max\left\{0,\ \mathcal{R} - \rho_{w(i)}^n\right\}, \qquad i = 1, 2, \ldots, N \tag{52}$$

with $w(i) = (i-1)M + 1$. When $\mathrm{dist}_{\overline{C}_w}\left(\overline{\mathbf{Z}}_T^n\right) = 0$,

$$\widetilde{\eta}_{i_n} = \max\left\{0,\ \mathcal{R} - \widetilde{\rho}_{w(i)}^n\right\}, \qquad i = 1, 2, \ldots, N, \tag{53}$$

and when $\mathrm{dist}_{\overline{C}_w}\left(\overline{\mathbf{Z}}_T^n\right) > 0$,

$$\widetilde{\eta}_{i_n}^{(1)} = \max\left\{0,\ \mathcal{R} - \widetilde{\rho}_{w1}^n\right\}, \qquad \widetilde{\eta}_{i_n}^{(2)} = \max\left\{0,\ \mathcal{R} - \widetilde{\rho}_{w2}^n\right\}, \qquad i = 1, 2, \ldots, N. \tag{54}$$

Here $\widetilde{\rho}_{w(i)}^n$ refers to the average of the scaled IBW function $\widetilde{\rho}\left(\theta, \tau_n\right)$ in cell $C_{w(i)}$, which is calculated in a similar way as (45). When the scaled IBW function is double-valued, the two average values are denoted as $\widetilde{\rho}_{w1}^n$ and $\widetilde{\rho}_{w2}^n$ $\left(\widetilde{\rho}_{w1}^n < \widetilde{\rho}_{w2}^n\right)$. In (51), $\overline{\mathbf{Z}}_T^n = \left(\mathcal{X}_n + \frac{\omega N}{2\pi}\tau_n, \mathcal{Y}_n\right)$ is the discrete tool center vector after scaling.

As for the PDE system, the terms $\bar{f}_{k+1/2}^n$, $\bar{f}_{k-1/2}^n$, and $\bar{\psi}_k^n$ in the FVM algorithm (46) are also computed using the tool center velocity $\dot{\mathbf{X}}_n = \left[\dot{\mathcal{X}}_n, \dot{\mathcal{Y}}_n\right]^{\mathrm{T}}$ at time step τ_n. Namely,

$$\begin{aligned} \bar{f}\left(\rho, \theta, \tau_n\right) &= -\omega\rho - \mathcal{V}_n \cos\left(\theta + \omega\tau_n + \Theta_0 + \Phi_n\right) \ln\rho \\ \bar{\psi}\left(\rho, \theta, \tau_n\right) &= \mathcal{V}_n \sin\left(\theta + \omega\tau_n + \Theta_0 + \Phi_n\right)\left(\ln\rho - 1\right), \end{aligned} \tag{55}$$

where

$$\mathcal{V}_n = \sqrt{\left(\dot{\mathcal{X}}_n + \frac{\omega N}{2\pi}\right)^2 + \dot{\mathcal{Y}}_n^2}, \qquad \tan\Phi_n = \dot{\mathcal{Y}}_n / \left(\dot{\mathcal{X}}_n + \frac{\omega N}{2\pi}\right). \tag{56}$$

The tool center velocity can be approximated as $\dot{\mathbf{X}}_n \approx \left(\mathbf{X}_n - \mathbf{X}_{n-1}\right)/\Delta\tau$ at each time step.

In summary, the mixed PDE–ODE system is solved by combining the FDM and FVM algorithms. The computational flowchart of the coupled algorithm is illustrated in Fig. 6.

5. Numerical results

An up-milling process illustrated in Fig. 7 is analyzed using both the proposed PDE–ODE formulation and the conventional DDE formulation [9]. The parameters used for the simulation of the two formulations are summarized in Table 1 [9,37]. The illustrative figure of the axial (a_p) and radial (a_e) depth of cut is given in Fig. 7(a). Mimicking the actual milling process, the tool does not touch the workpiece initially and is at a distance of $D_0 = 5.2\,\mathrm{mm}$. For the sake of simplicity, it is assumed that the two cutters are initially parallel to the Y-axis (see Fig. 7(b)).

To begin with, a convergence test of the proposed algorithm in Section 4 is conducted in Section 5.1. Then in Sections 5.2 and 5.3, the time domain simulation results and the steady-state tool vibrations predicted by the DDE and PDE–ODE formulations are compared, respectively. These comparison studies highlight the difference in the predicted behavior between the approximate DDE formulation and the proposed PDE–ODE model formulation. Moreover, the scenarios that cannot naturally be assessed using the DDE approach are investigated.

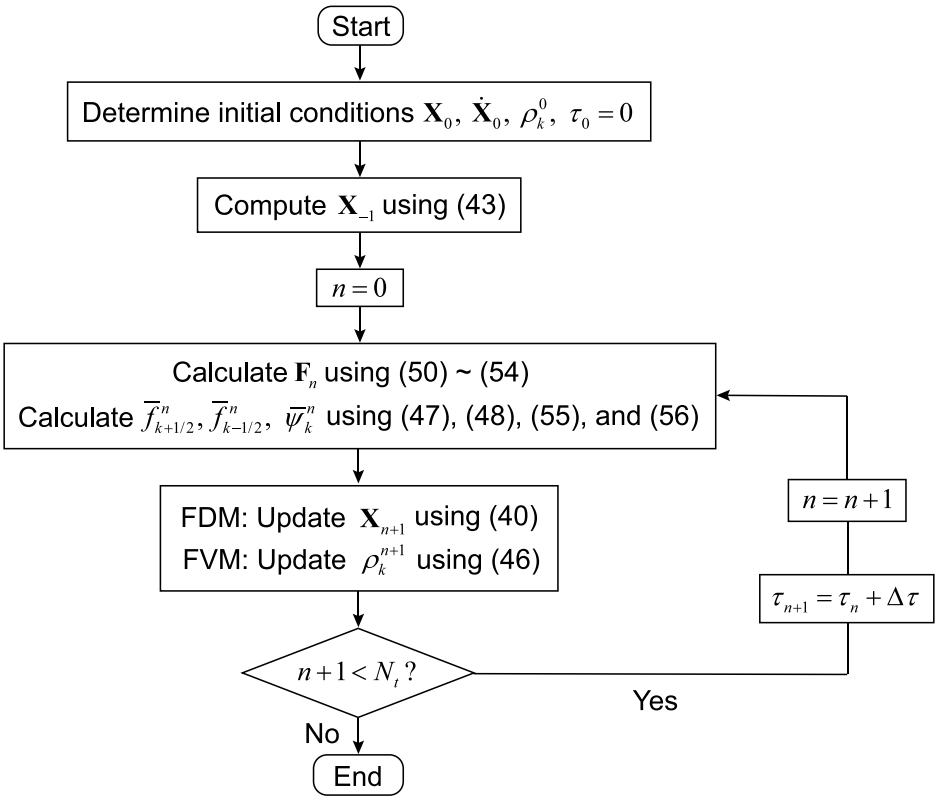

Fig. 6. The computational flowchart of solving the PDE–ODE system. N_t is the total number of time steps.

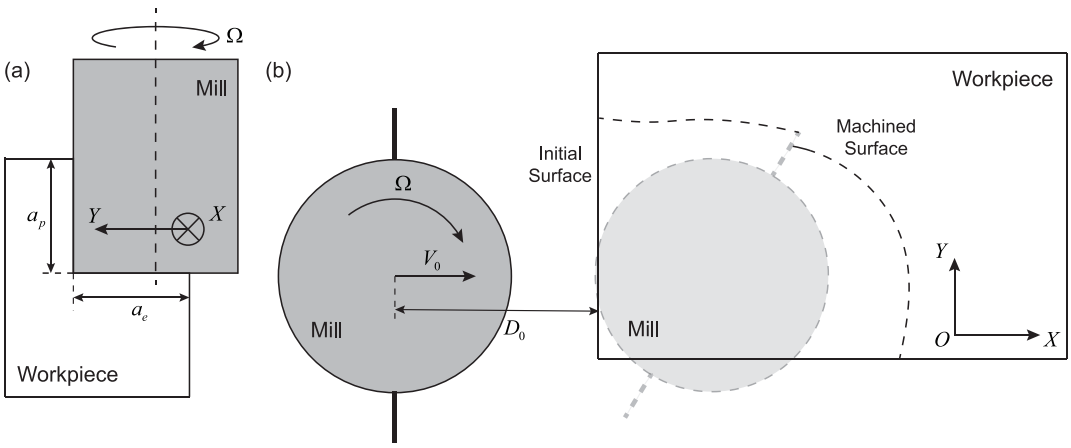

Fig. 7. Up-milling process: (a) side view and (b) top view. This is an illustrative figure where the lengths of a_e, a_p, and D_0 do not represent their physical lengths.

5.1. Convergence test of the numerical algorithm

Here we analyze the influence of the number of cells and of the CFL number on the simulation results obtained with the numerical algorithm introduced in Section 4. As illustrated in Fig. 8, the simulation results converge and become more accurate as these two numbers increase[4] However, the CFL number still needs to be less than 1 to guarantee convergence of the algorithm.

[4] The CFL number is in general only viewed as a criterion on convergence. However, according to [42], the first-order upwind scheme is more accurate when the CFL number is closer to 1.

Table 1
Parameters used for the simulation of the milling process.

Quantities	Parameters	Value	Unit
Lumped mass	M_X (M_Y)	0.02	kg
Lumped damper	C_X (C_Y)	27.62	N s/m
Lumped stiffness	K_X (K_Y)	3184.57	N/mm
Cutting coefficient	β	0.744	–
Cutting coefficient	K_t	462	$N/mm^{1+\beta}$
Cutting coefficient	K_r	38.6	$N/mm^{1+\beta}$
Radius of the mill	R	5	mm
Number of cutters	N	2	–
Feed per tooth	f_z	0.2	mm/tooth
Spindle speed	Ω	3×10^4	rpm
Axial depth of cut	a_p	1∼20	mm
Radial depth of cut	a_e	0.5/1/9/10	mm

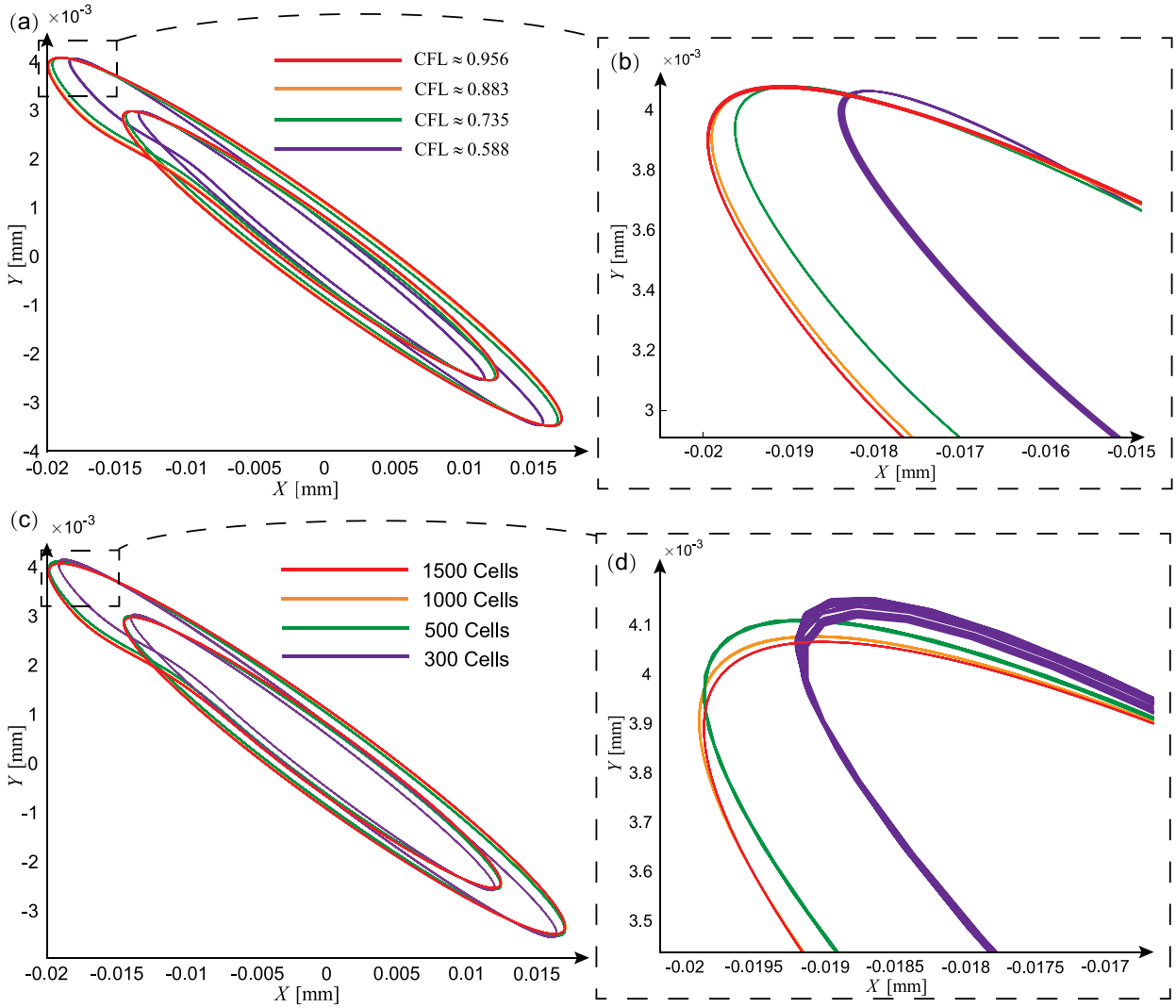

Fig. 8. Simulation results of the numerical algorithm under: (a–b) different CFL number and (c–d) different number of finite volumes.

5.2. Time-domain simulation results

As shown in Fig. 9(a), the tool center vibration along the X-axis, in the case of $a_e = 10$ mm, is simulated from $t = 0$ to $t = 0.14$ s. Other parameters used for the simulations are given in Table 1. A remarkable difference between the response of the PDE–ODE

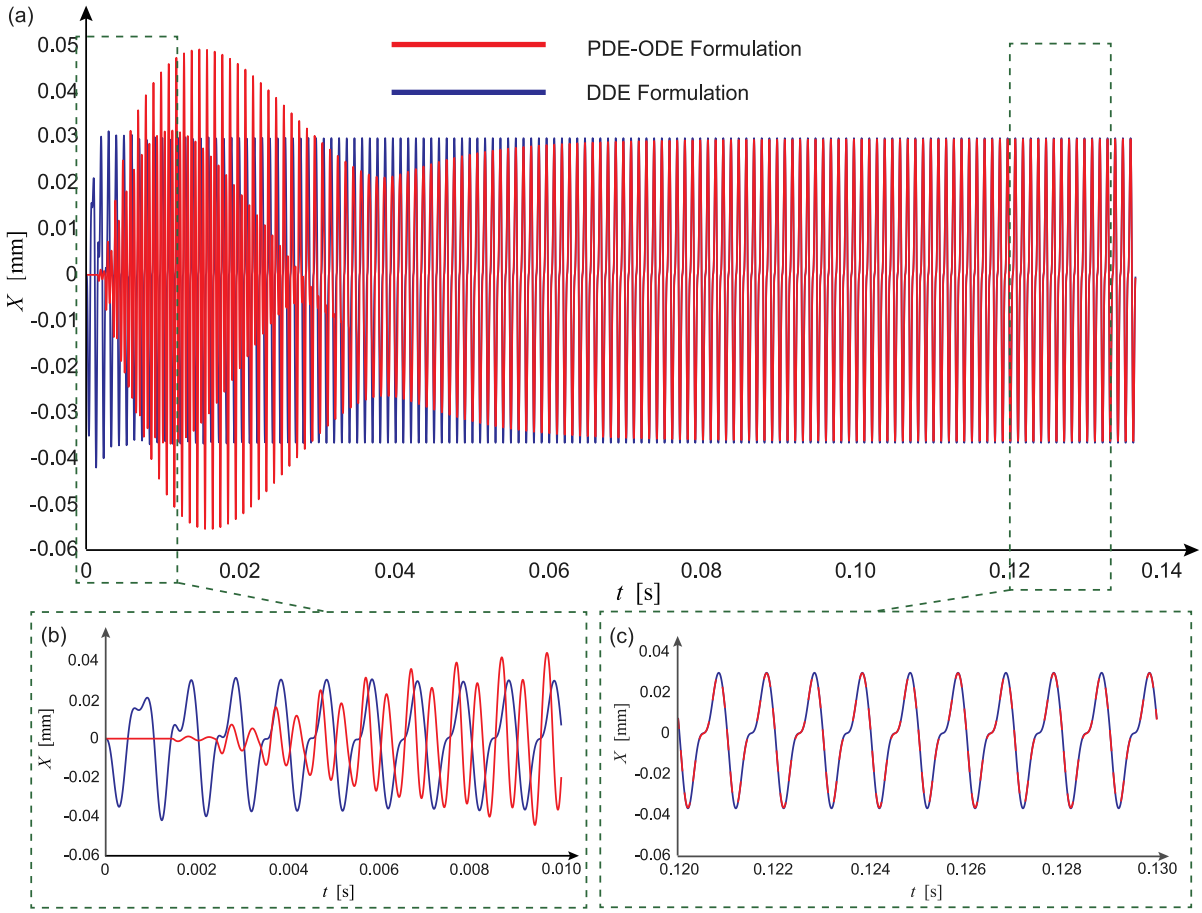

Fig. 9. (a) Tool center vibration in the X-direction when $\Omega = 30\,000$ rpm, $a_p = 1$ mm, and $a_e = 10$ mm (100% radial immersion): (b) simulation results from $t = 0$ to $t = 0.01$ s, and (c) simulation results from $t = 0.12$ s to $t = 0.13$ s.

model and the conventional DDE model occurs at the "early stage" ($t \in [0, 0.01\text{ s}]$) of the simulation, see Fig. 9(b). This difference occurs because the boundary of the workpiece significantly affects the chip thickness when the tool is milling the outer part of the workpiece [34], see Fig. 10. This "early stage" is not considered in the classical DDE formulation while it is naturally captured with the proposed PDE–ODE scheme. However, the influence of the boundary vanishes when the tool advances deep enough into the workpiece ($t \in [0.12, 0.13\text{ s}]$); after the "early stage" the two methods agree very well with each other, see Fig. 9(c). One advantage of the PDE–ODE formulation is demonstrated through this case: it is capable of simulating the tool dynamics throughout the milling process, especially when the tool is cutting the outer region of the workpiece and the chip thickness is strongly influenced by the initial shape of the workpiece.

In this example, only one of the two cutters is engaged with the workpiece, causing the cutting force F_{ti} on the other cutter to drop to zero, see Fig. 11.

5.3. Steady-state tool vibration

In this section, steady-state tool vibration characterized by limit cycles, reflecting the periodic motions of the tool center, are predicted by both methods and these results are compared. Fig. 12 illustrates the limit cycles at a small axial depth of cut $a_p = 1$ mm, and at the following four different radial depths of cut: (a) $a_e = 10$ mm, 100% radial immersion, (b) $a_e = 9$ mm, 90% radial immersion, (c) $a_e = 1$ mm, 10% radial immersion, and (d) $a_e = 0.5$ mm, 5% radial immersion. It is shown that the radial depth of cut has a strong influence on the shapes of the limit cycles. Under this small axial depth of cut ($a_p = 1$ mm), the difference between the two formulations (i.e., the error E of the DDE-based model with respect to the PDE–ODE model) is small, see Table 2. However, the limit cycle is very small at the radial depth of cut $a_e = 0.5$ mm, and thus the relative error E_r in this case becomes large (10.4%). As a result, the difference between the two formulations looks more remarkable in Fig. 12(d).

Here the error E and the relative error E_r are respectively defined as:

$$E = \frac{1}{N_r}\sum_{i=1}^{N_r}\sqrt{\left(X_D\left(t_i\right) - X_P\left(t_i\right)\right)^2 + \left(Y_D\left(t_i\right) - Y_P\left(t_i\right)\right)^2}, \tag{57}$$

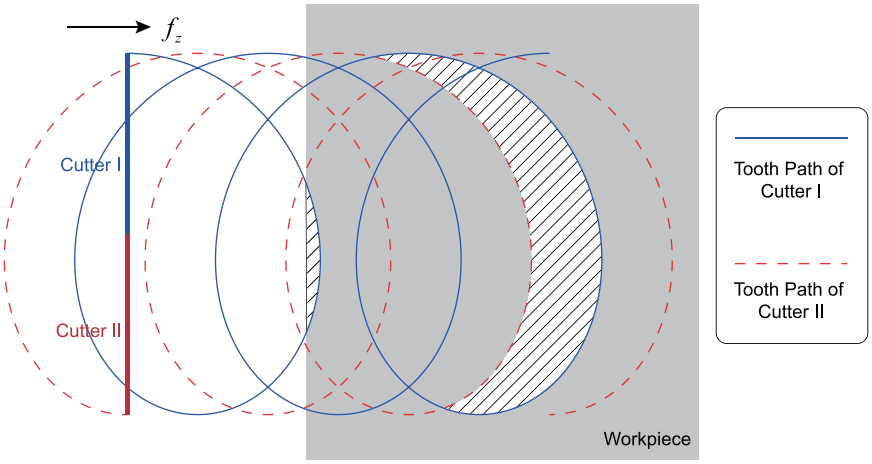

Fig. 10. The initial shape of the workpiece can significantly affect the chip thickness when the tool is milling the outer region of the workpiece. *Source:* Adopted from [34].

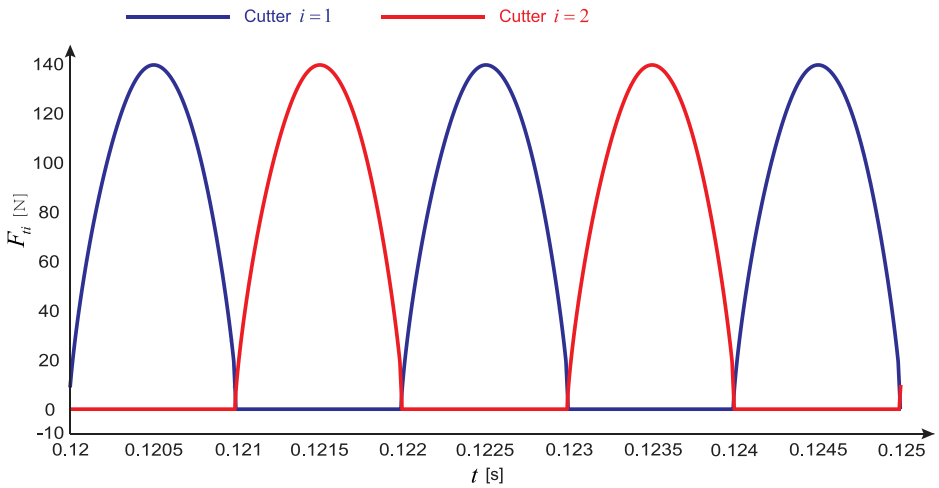

Fig. 11. Cutting forces F_{ti} on the two cutters as functions of time.

Table 2
The errors and relative errors of the DDE-based model with respect to the PDE–ODE model under different radial depth of cut.

	$a_e = 10$ mm	$a_e = 9$ mm	$a_e = 1$ mm	$a_e = 0.5$ mm
Error E of the DDE-based model [mm]	1.87×10^{-4}	1.30×10^{-3}	5.02×10^{-4}	6.35×10^{-4}
Relative Error E_r of the DDE-based model [–]	0.83%	7.0%	5.0%	10.4%

$$E_r = \frac{1}{N_r} \sum_{i=1}^{N_r} \frac{\sqrt{\left(X_D\left(t_i\right) - X_P\left(t_i\right)\right)^2 + \left(Y_D\left(t_i\right) - Y_P\left(t_i\right)\right)^2}}{\sqrt{X_P^2\left(t_i\right) + Y_P^2\left(t_i\right)}}, \tag{58}$$

where $\left[X_D\left(t_i\right), Y_D\left(t_i\right)\right]$ and $\left[X_P\left(t_i\right), Y_P\left(t_i\right)\right]$ are tool center positions predicted by the DDE formulation and the PDE–ODE formulation at each time step t_i, and N_r is the total number of time steps evaluated.

When the axial depth of cut increases to $a_p = 20$ mm (radial depth of cut $a_e = 0.5$ mm), the difference between the two formulations becomes substantial ($E = 0.0231$ mm), see Fig. 13. Under the same radial depth of cut $a_e = 0.5$ mm, the limit cycle is similar to that in Fig. 12(d) but of a larger size.

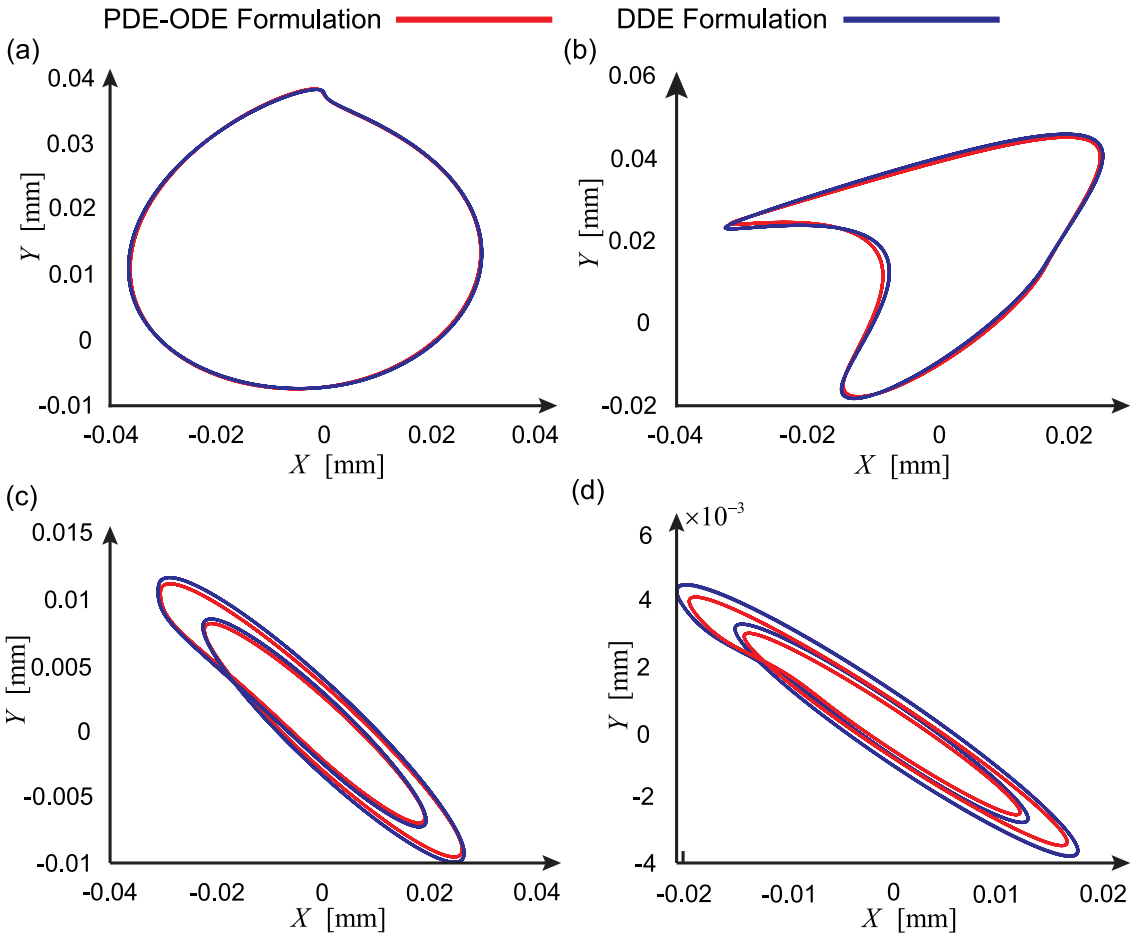

Fig. 12. Limit cycles of tool center under different radial depth of cut: (a) $a_e = 10\,\text{mm}$, 100% radial immersion, (b) $a_e = 9\,\text{mm}$, 90% radial immersion, (c) $a_e = 1\,\text{mm}$, 10% radial immersion, and (d) $a_e = 0.5\,\text{mm}$, 5% radial immersion. The spindle speed is $\Omega = 30\,000\,\text{rpm}$, and the axial depth of cut is $a_p = 1\,\text{mm}$.

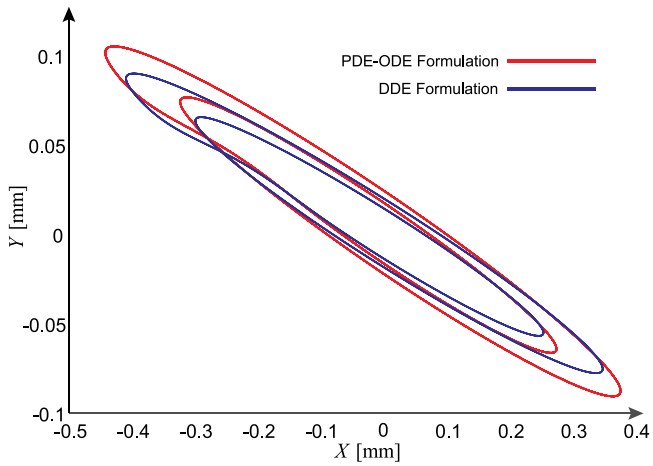

Fig. 13. Comparison of the limit cycles computed using the PDE–ODE formulation and a conventional DDE formulation [9]. The spindle speed $\Omega = 30\,000\,\text{rpm}$, axial depth of cut $a_p = 20\,\text{mm}$, and radial depth of cut $a_e = 0.5\,\text{mm}$ (5% radial immersion).

Let us now investigate the underlying reason for these differences — the simplified chip thickness model used in the DDE formulation. First, the approximated chip thickness model in the DDE formulation in [9] can be written as[5]

$$h_i(t) = \sin\phi_i(t)\left[X_T(t) - X_T\left(t-\tau_i\right)\right] + \cos\phi_i(t)\left[Y_T(t) - Y_T\left(t-\tau_i\right)\right] + R - R\cos\left(\Omega\tau_i - \theta\right) \tag{59}$$

with

$$\tau_i = \frac{\hat{\tau}\theta R}{f_z\cos\phi_i(t) + \theta R}, \qquad \theta = \frac{2\pi}{N}, \qquad \hat{\tau} = \frac{\theta}{\Omega}. \tag{60}$$

In contrast, the exact chip thickness should be the minimum non-negative value of a series of "possible chip thickness" values

$$h_i(t) = \max\left\{0, \min_j\left\{h_i^j(t)\right\}\right\}, \tag{61}$$

where the "possible chip thickness" $h_i^j(t)$ is determined by assuming the milled surface is left by a previous cutter j and is given by

$$h_i^j(t) = \sin\phi_i(t)\left[X_T(t) - X_T\left(t-\tau_i^j\right)\right] + \cos\phi_i(t)\left[Y_T(t) - Y_T\left(t-\tau_i^j\right)\right] + R - R\cos\left(\Omega\tau_i^j - j\theta\right), \tag{62}$$

where the time delay τ_i^j is determined implicitly through the nonlinear equation

$$\cos\phi_i(t)\left[X_T(t) - X_T\left(t-\tau_i^j\right)\right] - \sin\phi_i(t)\left[Y_T(t) - Y_T\left(t-\tau_i^j\right)\right] + R\sin\left(\Omega\tau_i^j - j\theta\right) = 0. \tag{63}$$

Comparing with the simplified chip thickness model in (59), the exact chip thickness model in (61) considers more previous cutters because of the fact that the chip thickness is not always determined by the position difference between two subsequent cutters. Moreover, the exact chip thickness model uses the exact time delay τ_i^j determined by (63) to compute the chip thickness, rather than using the approximate one in (60). Correspondingly, this exact chip thickness model degenerates to the simplified one in by considering only one non-negative chip thickness ($j = 1$) and using the estimated time delay in (60) as an approximate solution of (63). More details of the proposed exact chip thickness model is provided in Appendix C.

Second, the DDE formulation in [9] introduces entry (ϕ_s) and exist (ϕ_e) angles and modify the cutting force model (4) to

$$F_{ti} = K_t a_p h_i^\beta(t)\, g\left(\phi_i(t)\right), \qquad F_{ri} = K_r a_p h_i^\beta(t)\, g\left(\phi_i(t)\right), \qquad i = 1, 2, \ldots, N, \tag{64}$$

with

$$g_i\left(\phi_i(t)\right) = \begin{cases} 1, & \phi_s \le \phi_i(t) \le \phi_e \wedge h_i(t) > 0 \\ 0, & \text{otherwise}. \end{cases} \tag{65}$$

This is done because the non-negative requirement of the chip thickness is not guaranteed in the simplified model (59), which can result in an unrealistic cutting force. In [9], this problem is solved by predetermining a specific range of orientations — the chip thickness is positive when the cutters align to these directions. The chip thickness computed by (59) is adopted only when it is positive and when the cutter is within the proposed range of orientations; otherwise the chip thickness (cutting force) is set to zero. This procedure is mathematically conducted through the discontinuous function $g_i\left(\phi_i(t)\right)$ and thus the non-negative characteristic of the chip thickness is satisfied. As illustrated in Fig. 14, the range is defined from ϕ_s to ϕ_e, with

$$\phi_s = -\frac{\theta f_z}{2\left(f_z + \theta R\right)}, \qquad \phi_e = \arccos\left(\frac{R - a_e}{R}\right), \tag{66}$$

where a_e is the radial depth of cut.

However, this procedure introduces errors when the cutter reaches Region A in Fig. 14: the cutter is still removing material but the cutting force is artificially set to zero according to (65) in the DDE model formulation. From another perspective, this error can be interpreted as the chip thickness being set to zero too early.

As illustrated in Fig. 15, the above two errors of the DDE-based model are small (and potentially negligible) when the scaled depth of cut $\mathcal{P}$ is relatively small ($\mathcal{P} < \mathcal{P}_*$). However, when $\mathcal{P}$ is larger than the threshold number $\mathcal{P}_* \approx 1.65$ for the particular problem considered here, the error of the DDE-based model increases with $\mathcal{P}$.

Physically, this reflects that when the depth of cut a_p increases, even a small error in the chip thickness is amplified while computing the cutting force (see (4)), which can result in increasing errors on the limit cycle characterizing the actual tool vibration. Moreover, when we eliminate the errors in the DDE-based model by using the exact chip thickness model in (61) to (63) and the cutting force model in (4), the improved model agrees very well with the PDE–ODE formulation. More details are provided in Appendix C.

In summary, the PDE–ODE formulation provides an accurate prediction of tool dynamics and can be viewed as a reference solution for the DDE formulation. The approximate DDE formulation is computationally more efficient in general. However, the PDE–ODE formulation is more reliable in some extreme scenarios and is more computationally efficient than the DDE model, if the latter is extended with the exact chip thickness model (see Appendix C).

[5] Here the chip thickness model used in the DDE formulation is rewritten in a new form for a better illustration of its connection with the proposed exact formulation in (62). More details are provided in Appendix B.

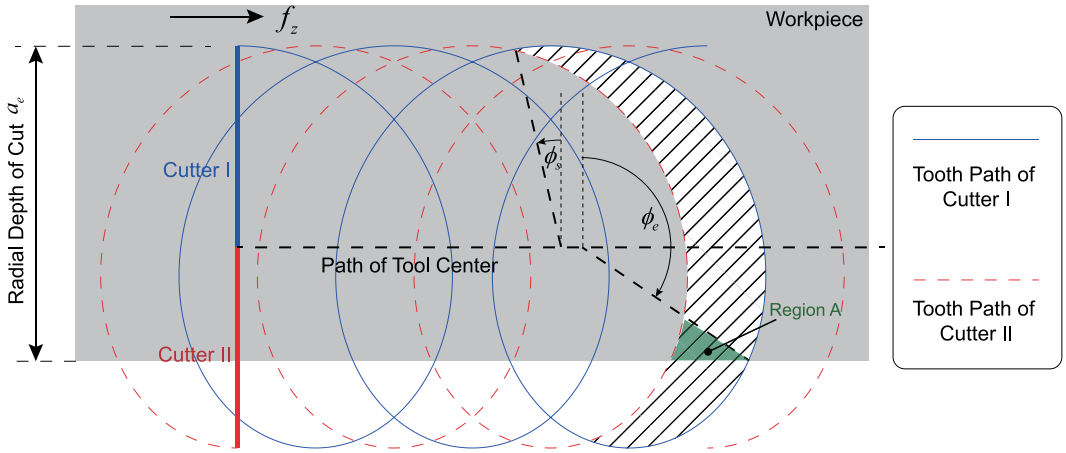

Fig. 14. Entry and exit angles in an up-milling process. The cutter is still removing materials in Region A.

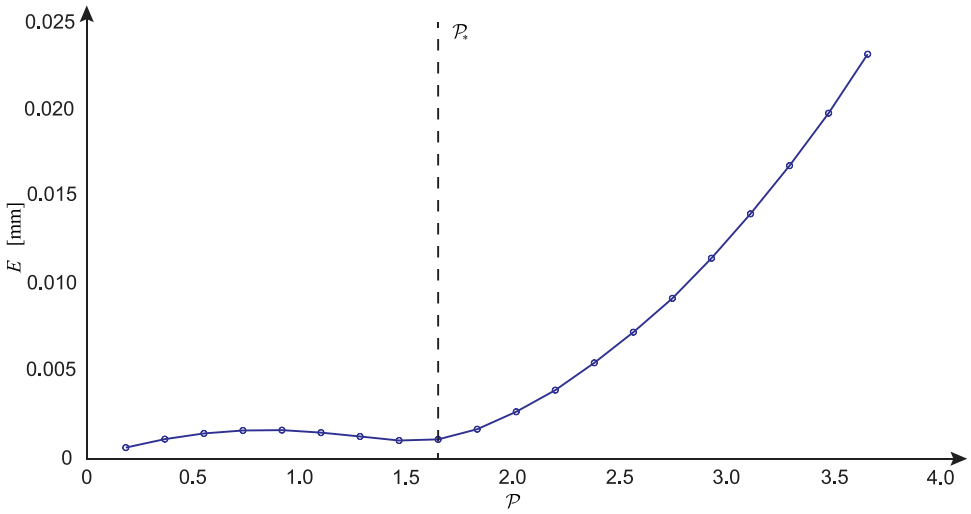

Fig. 15. Errors of a DDE-based model at different scaled depth of cut $\mathcal{P}$.

6. Conclusions

In this article, a mathematical formulation is established for a class of milling models that consider both the motion of the tool and the evolution of the machined surface. In this formulation, the chip thickness is defined exactly using a surface function that describes the milled surface around the tool and the information about the workpiece boundary. Coupling of the partial differential equation (PDE) governing the evolution of the surface function with the ordinary differential equations (ODE) describing tool/machine dynamics results in a system of PDE–ODE. The scaled PDE–ODE is solved using an algorithm combining the finite volume method and the finite difference method. A case study illustrates two advantages of the proposed model formulation: (i) it has a theoretically exact chip thickness model and can help delimit the range of validity of the conventional delay differential equations (DDE) formulation; (ii) it is capable of simulating the transient tool dynamics while milling the outer region of the workpiece, which is often neglected by the DDE formulation. This formulation serves as the mathematical background of a class of milling models and provides a novel perspective of analyzing the milling process. Future research will focus on the possible applications of the proposed PDE–ODE model formulation, in particular stability analysis, surface finish evaluation, and controller design.

CRediT authorship contribution statement

Kaidong Chen: Conceptualization, Methodology, Software, Validation, Writing – original draft. **He Zhang:** Methodology, Writing – review & editing. **Nathan van de Wouw:** Conceptualization, Methodology, Supervision, Writing – review & editing. **Emmanuel Detournay:** Conceptualization, Methodology, Supervision, Writing – review & editing.

Declaration of competing interest

The authors declare that they have no known competing financial interests or personal relationships that could have appeared to influence the work reported in this paper.

Data availability

No data was used for the research described in the article.

Appendix A. Brief physical explanations on the evolution of the surface function

This appendix provides a brief physical interpretation of the PDE [34] governing the evolution of the surface function, introduced in Section 2.2.1:

$$\frac{\partial r}{\partial t} + \frac{\partial f}{\partial \theta} = \psi \,, \tag{A.1}$$

where

$$\begin{aligned} f\left(r,\,\theta,\,t\right) &= -\Omega r - V\cos\left(\theta + \Omega t + \Theta_0 + \Phi\right)\ln r \\ \psi\left(r,\,\theta,\,t\right) &= V\sin\left(\theta + \Omega t + \Theta_0 + \Phi\right)\left[\ln r - 1\right] \,. \end{aligned} \tag{A.2}$$

As illustrated in Fig. A.1, the surface function $r(\theta,\,t_0)$ describes the shape of the surface of the workpiece around the tool at time t_0, defined with respect to the center of the tool. Let us now focus on the surface function in a specific direction θ; its value changes when the tool center moves laterally and when the mill rotates around its axis. Specifically, this process is governed by the following two categories of relative movements.

First, the surface function evolves when the tool rotates relatively with respect to the workpiece. This relative rotation is caused by the self-rotation of the mill (Ω) as well as by the tangential motion of the tool center, see Fig. A.1(b). The tangential component of the velocity of the tool center is $V_t = V\sin(\theta + \Omega t + \Theta_0 + \Phi - \pi/2) = -V\cos(\theta + \Omega t + \Theta_0 + \Phi)$. Here $V = \|\mathbf{V}\|$ is the magnitude of velocity of the tool center $\mathbf{V}$. From this perspective, function f in (A.2) can be rewritten as: $f = -\Omega r + V_t \ln r$, which describes the relative rotation of the tool with respect to the workpiece.

Second, the radial movement between the tool and the workpiece also influences the value of the surface function, see Fig. A.1(c). The radial component of the velocity of the tool center is $V_r = V\cos(\theta + \Omega t + \Theta_0 + \Phi - \pi/2) = V\sin(\theta + \Omega t + \Theta_0 + \Phi)$. Similarly, ψ in (A.2) can be rewritten as: $\psi = V_r(\ln r - 1)$, which is associated with the radial movement of the tool with respect to the workpiece.

In summary, (A.1) reflects that the evolution of the surface function is governed by the rotation of the tool and by the motion of its center relative to the workpiece.

In above analysis, the term $\theta + \Omega t + \Theta_0 + \Phi - \pi/2$ is the angle between the velocity of the tool center and the orientation θ measured in the (x, y) frame. As illustrated in Fig. A.1(d), two frames are considered in our research: (i) the global frame (X, Y) and the local frame (x, y) rotating with the mill at a constant spindle speed of Ω. At time t, the angle between the two frames is $\Omega t + \Theta_0$, where Θ_0 is the initial angle. The velocity of the tool center $\mathbf{V}$ is measured in the global frame (X, Y), and its angle with respect to the X-axis is Φ. In contrast, the orientation θ is defined in the local frame (x, y), and its angle with respect to the y-axis is θ. Through Fig. A.1(d), the angle between the velocity of the tool center and the orientation θ is obtained as $\theta + \Omega t + \Theta_0 + \Phi - \pi/2$.

Appendix B. The approximated chip thickness model in the DDE model formulation

In [9], the chip thickness model reads

$$h = h_s + h_d \tag{B.1}$$

with

$$h_s = R - R\cos\left(\Omega\tau_i - \theta\right) + \frac{f_z}{\hat{\tau}}\tau_i \sin\phi_i\left(t\right) \,, \quad h_d = \sin\phi_i\left(t\right)\left[X_d\left(t\right) - X_d\left(t - \tau_i\right)\right] + \cos\phi_i\left(t\right)\left[Y_d\left(t\right) - Y_d\left(t - \tau_i\right)\right] \,. \tag{B.2}$$

$$\tau_i = \frac{\hat{\tau}\theta R}{f_z\cos\phi_i\left(t\right) + \theta R} \,, \qquad \theta = \frac{2\pi}{N} \,, \qquad \hat{\tau} = \frac{\theta}{\Omega} \,, \qquad i = 1,\,2,\,\ldots,\,N \,. \tag{B.3}$$

Here $\left[X_d\left(t\right),\,Y_d\left(t\right)\right]$ describes the (perturbed) vibration of the tool center with respect to the prescribed movement of the tool:

$$\begin{bmatrix} X_d\left(t\right) \\ Y_d\left(t\right) \end{bmatrix} = \begin{bmatrix} X_T\left(t\right) \\ Y_T\left(t\right) \end{bmatrix} - \begin{bmatrix} V_0 t \\ 0 \end{bmatrix} \,. \tag{B.4}$$

Given the fact that $f_z = \frac{2\pi V_0}{N\Omega}$, the last term of h_s can be rewritten as

$$\frac{f_z}{\hat{\tau}}\tau_i \sin\phi_i\left(t\right) = V_0\tau_i\sin\phi_i\left(t\right) = \left[V_0 t - V_0\left(t - \tau_i\right)\right]\sin\phi_i\left(t\right) \,. \tag{B.5}$$

By substituting (B.2), (B.4), and (B.5) into (B.1), the chip thickness model is rewritten as

$$h = \sin\phi_i\left(t\right)\left[X_T\left(t\right) - X_T\left(t - \tau_i\right)\right] + \cos\phi_i\left(t\right)\left[Y_T\left(t\right) - Y_T\left(t - \tau_i\right)\right] + R - R\cos\left(\Omega\tau_i - \theta\right) \,. \tag{B.6}$$

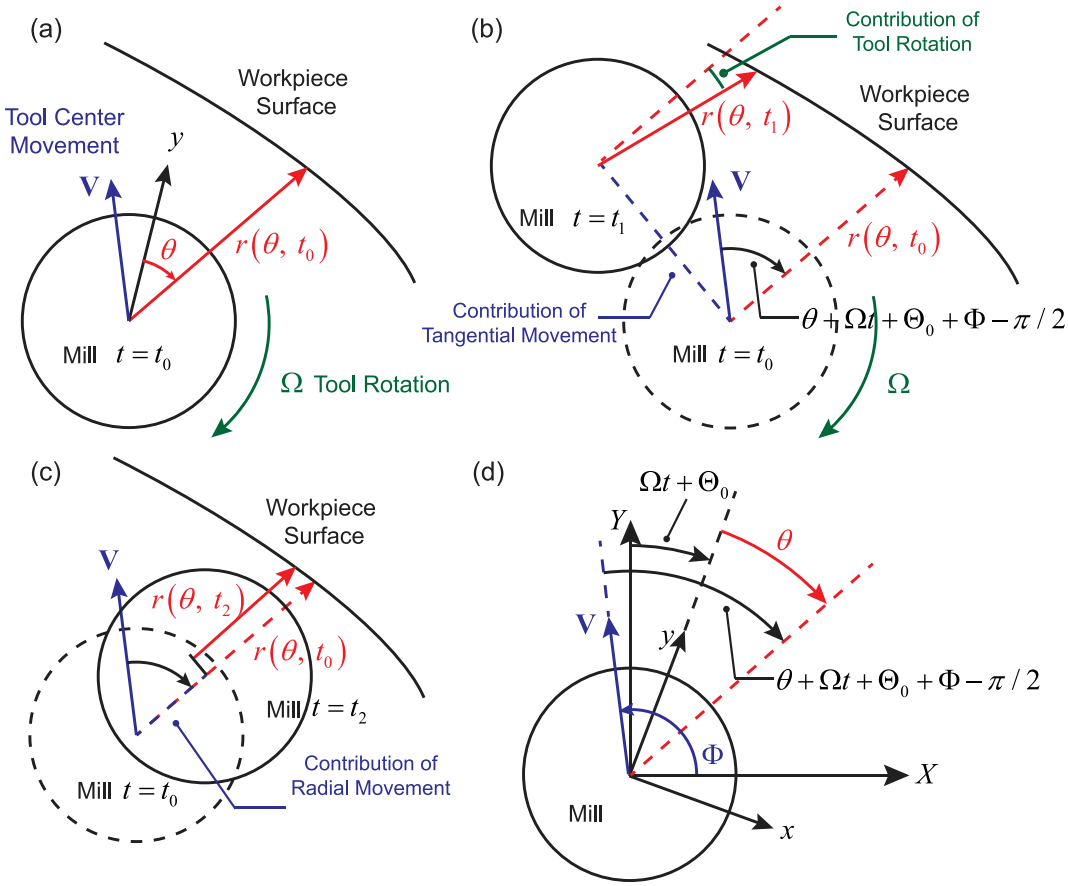

Fig. A.1. Illustrative figure of the physical explanation on the PDE governing the evolution of the surface function. (a) Original surface function. (b) Surface function evolution caused by the relative rotation of the mill with respect to the workpiece. (c) Surface function evolution caused by the radial movement of the mill with respect to the workpiece. (d) The angle between the velocity of the tool center **V** and orientation θ defined in the (x, y) frame.

Appendix C. An exact chip thickness model for Class I models

In this appendix, we determine the chip thickness in milling from the perspective of Class I models without any simplifications. As illustrated in Fig. C.1, Class I models assume that the current material ahead of cutter i is left by a specific preceding cutter j. With given cutter i and given index j, the orientation of cutter j is specified through

$$\theta_j = \mod\left(\theta_i + j\theta, 2\pi\right), \tag{C.1}$$

where θ_i and θ_j are the orientations of cutters i and j measured in (x, y) frame fixed to the mill, and $\theta = \frac{2\pi}{N}$ is the angle between two neighboring cutters. The modulus function $m(x) = \mod(x, 2\pi)$ is defined as follows:

$$y = m(x) = \mod(x, 2\pi) \Leftrightarrow y = x - 2k\pi, \quad y \in [0, 2\pi), \quad k \in \mathbb{Z}. \tag{C.2}$$

After considering all the possible $j = 1, 2, 3\ldots$, the minimum non-negative chip thickness is the true value

$$h_i(t) = \max\left\{0, \min_j\left\{h_i^j(t)\right\}\right\}, \tag{C.3}$$

where $h_i^j(t)$ is the possible chip thickness corresponding to the difference in the positions of cutter i and cutter j.

The following describes the procedure to determine $h_i^j(t)$. As illustrated in Fig. C.1, the position of point J is the sum of the position of point C_j and the relative position of point J with respect to C_j. C_j is the position of tool center at time t_j and the distance between point C_j and point J is $\overline{C_jJ} = R$. Therefore, the coordinates of point J in the global frame are given by:

$$\mathbf{X}_J = \begin{bmatrix} X_J \\ Y_J \end{bmatrix} = \begin{bmatrix} X_{C_j} \\ Y_{C_j} \end{bmatrix} + \begin{bmatrix} R\sin\phi_j \\ R\cos\phi_j \end{bmatrix} = \begin{bmatrix} X_T\left(t_j\right) + R\sin\phi_j \\ Y_T\left(t_j\right) + R\cos\phi_j \end{bmatrix}. \tag{C.4}$$

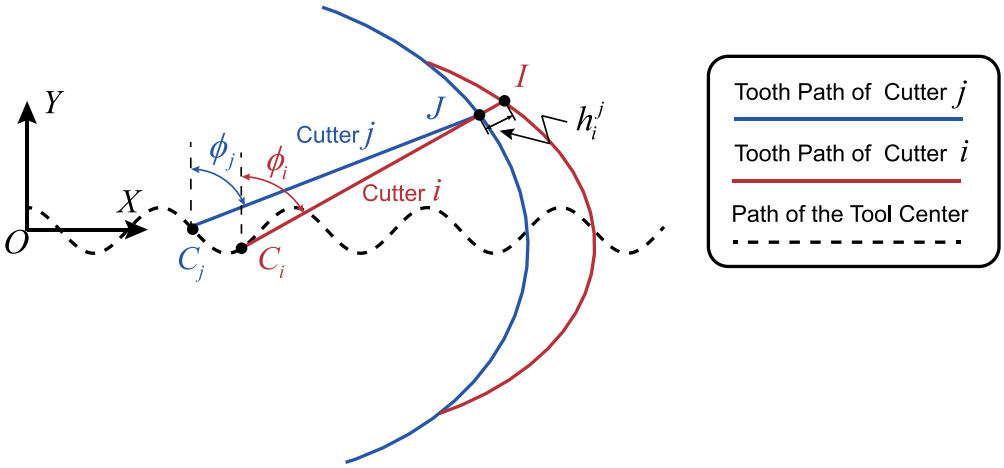

Fig. C.1. Geometric illustration for the formation of the chip thickness.

On the other hand, the position of point J can also be viewed as the sum of the position of point C_i and the relative position of point J with respect to C_i. C_i is the position of tool center at current time t and the distance between point C_i and point J is $\overline{C_iJ} = R - h_i^j$. As such, the following expression for the coordinates of point J can be given:

$$\mathbf{X}_J = \begin{bmatrix} X_J \\ Y_J \end{bmatrix} = \begin{bmatrix} X_{C_i} \\ Y_{C_i} \end{bmatrix} + \begin{bmatrix} \left(R - h_i^j\right)\sin\phi_i \\ \left(R - h_i^j\right)\cos\phi_i \end{bmatrix} = \begin{bmatrix} X_T(t) + \left(R - h_i^j\right)\sin\phi_i \\ Y_T(t) + \left(R - h_i^j\right)\cos\phi_i \end{bmatrix}. \tag{C.5}$$

By equating (C.4) and (C.5), we have

$$\begin{aligned} X_T\left(t_j\right) + R\sin\phi_j &= X_T(t) + \left(R - h_i^j\right)\sin\phi_i \\ Y_T\left(t_j\right) + R\cos\phi_j &= Y_T(t) + \left(R - h_i^j\right)\cos\phi_i\,, \end{aligned} \tag{C.6}$$

from which the chip thickness can be solved as

$$h_i^j = \sin\phi_i\left[X_T(t) - X_T\left(t_j\right)\right] + \cos\phi_i\left[Y_T(t) - Y_T\left(t_j\right)\right] + R - R\cos\left(\phi_i - \phi_j\right)\,, \tag{C.7}$$

where ϕ_i (ϕ_j) is the angle between cutter i (j) and the Y-axis:

$$\phi_i = \Omega t + \Theta_0 + \theta_i\,, \qquad \phi_j = \Omega t_j + \Theta_0 + \theta_j\,. \tag{C.8}$$

Substitute (C.8) and (C.1) into (C.7), and introduce time delay $\tau_i^j = t - t_j$,[6] the chip thickness model becomes

$$h_i^j = \sin\phi_i\left[X_T(t) - X_T\left(t - \tau_i^j\right)\right] + \cos\phi_i\left[Y_T(t) - Y_T\left(t - \tau_i^j\right)\right] + R - R\cos\left(\Omega\tau_i^j - j\theta\right)\,. \tag{C.9}$$

In order to determine the time delay τ_i^j, we eliminate term $\left(R - h_i^j\right)$ in (C.6)

$$\cos\phi_i\left[X_T(t) - X_T\left(t_j\right)\right] - \sin\phi_i\left[Y_T(t) - Y_T\left(t_j\right)\right] + R\sin\left(\phi_i - \phi_j\right) = 0 \tag{C.10}$$

Again substitute (C.8) and (C.1) into (C.10); then we have

$$\cos\phi_i\left[X_T(t) - X_T\left(t - \tau_i^j\right)\right] - \sin\phi_i\left[Y_T(t) - Y_T\left(t - \tau_i^j\right)\right] + R\sin\left(\Omega\tau_i^j - j\theta\right) = 0\,, \tag{C.11}$$

which is an implicit equation through which the time delay τ_i^j can be solved

In summary, the chip thickness model is determined without any simplifications in the form

$$h_i = \max\left\{0,\ \min_j\left\{h_i^j\right\}\right\}\,, \tag{C.12}$$

$$h_i^j = \sin\phi_i\left[X_T(t) - X_T\left(t - \tau_i^j\right)\right] + \cos\phi_i\left[Y_T(t) - Y_T\left(t - \tau_i^j\right)\right] + R - R\cos\left(\Omega\tau_i^j - j\theta\right)\,, \tag{C.13}$$

and the time delay τ_i^j is determined implicitly through

$$\cos\phi_i\left[X_T(t) - X_T\left(t - \tau_i^j\right)\right] - \sin\phi_i\left[Y_T(t) - Y_T\left(t - \tau_i^j\right)\right] + R\sin\left(\Omega\tau_i^j - j\theta\right) = 0\,. \tag{C.14}$$

[6] Here τ_i^j depends on i in the sense that time t refers to the instance when a given cutter i is engaged with the workpiece.

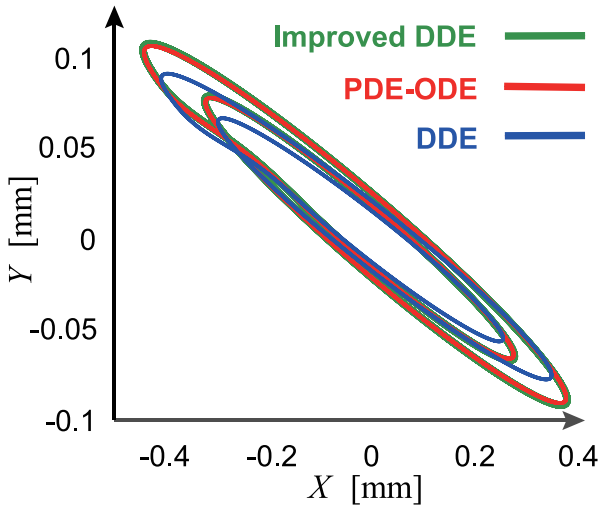

Fig. C.2. Limit cycles computed by the PDE–ODE formulation and the DDE formulation [9] using simplified and improved chip thickness models. The spindle speed $\Omega = 30\,000\,\mathrm{rpm}$, axial depth of cut $a_p = 20\,\mathrm{mm}$, and radial immersion $a_e = 0.5\,\mathrm{mm}$ (5%).

Table C.1
CPU times of the PDE–ODE formulation and the improved DDE model for tools with different numbers of cutters. The spindle speed $\Omega = 30\,000\,\mathrm{rpm}$, axial depth of cut $a_p = 20\,\mathrm{mm}$, and radial immersion $a_e = 0.5\,\mathrm{mm}$ (5%).

	2 Cutters	3 Cutters	4 Cutters
CPU time of the PDE–ODE formulation [s]	13.1	13.0	13.0
CPU time of the improved DDE model [s]	18.9	28.2	36.0

Finally, the possible influence from the boundary of the workpiece is considered following the same procedure in Section 2.2.4. The chip thickness in (C.12) is further modified to

$$\overline{h}_i = \begin{cases} \max\left\{0,\, h_i - \widetilde{h}_i\right\}, & \mathrm{dist}_{C_w}\left(\mathbf{Z}_T\right) = 0 \\ \max\left\{0,\, \min\left\{h_i,\, \widetilde{h}_i^{(1)}\right\} - \widetilde{h}_i^{(2)}\right\}, & \mathrm{dist}_{C_w}\left(\mathbf{Z}_T\right) > 0\,. \end{cases} \tag{C.15}$$

As illustrated in Fig. C.2, replacing the simplified chip thickness model in [9] with the improved chip thickness model (C.15) results in an excellent agreement with the PDE–ODE formulation.

However, this improved DDE-based model can be computationally intensive because the nonlinear equation (C.14) need to be solved at each time step. Moreover, the suitable number of preceding cutters to be considered remains an open problem. While simulating the proposed case for 50 000 time steps, the CPU time of the PDE–ODE formulation and the improved model (considering two preceding cutters) are respectively 13.1 s and 18.9 s. When the number of cutters increases, the computational load of the improved DDE model increases significantly while the PDE–ODE formulation is not affected, see Table C.1.

References

[1] Y. Altintas, Manufacturing Automation: Metal Cutting Mechanics, Machine Tool Vibrations, and CNC Design, Cambridge University Press, 2012.
[2] L.N. López de lacalle, J. Pérez, J.I. Llorente, J.A. Sánchez, Advanced cutting conditions for the milling of aeronautical alloys, J. Mater Process. Technol. 100 (1–3) (2000) 1–11.
[3] R. Piquard, A. D'Acunto, P. Laheurte, D. Dudzinski, Micro-end milling of NiTi biomedical alloys, burr formation and phase transformation, Precis. Eng. 38 (2) (2014) 356–364.
[4] C.N. Chu, S.Y. Kim, J.M. Lee, B.H. Kim, Feed-rate optimization of ball end milling considering local shape features, CIRP Ann. 46 (1) (1997) 433–436.
[5] Z. Wang, C. Li, M. Xu, Y. Zhang, Dynamic analysis and stability prediction of nonlinear feed system coupled with flexible workpiece, J. Sound Vib. 520 (2022) 116597.
[6] F. Defant, D. Ghezzi, P. Albertelli, Development of a generalized extended harmonic solution for analyzing the combination of chatter suppression techniques in milling, J. Sound Vib. 543 (2023) 117368.
[7] S.A. Tobias, W. Fishwick, Theory of regenerative machine tool chatter, Engineer 205 (7) (1958) 199–203.
[8] H. Paris, G. Peigne, R. Mayer, Surface shape prediction in high speed milling, Int. J. Mach. Tools Manuf. 44 (15) (2004) 1567–1576.
[9] R.P.H. Faassen, N. van de Wouw, H. Nijmeijer, J.A.J. Oosterling, An improved tool path model including periodic delay for chatter prediction in milling, J. Comput. Nonlinear Dyn. 2 (2) (2006) 167–179, http://dx.doi.org/10.1115/1.2447465.
[10] S.D. Merdol, Y. Altintas, Multi frequency solution of chatter stability for low immersion milling, J. Manuf. Sci. Eng. 126 (3) (2004) 459–466.
[11] T. Insperger, J. Gradišek, M. Kalveram, G. Stépán, K. Winert, E. Govekar, Machine tool chatter and surface location error in milling processes, J. Manuf. Sci. Eng. 128 (4) (2006) 913–920, http://dx.doi.org/10.1115/1.2280634.

[12] K. Li, K. Zhu, T. Mei, A generic instantaneous undeformed chip thickness model for the cutting force modeling in micromilling, Int. J. Mach. Tools Manuf. 105 (2016) 23–31.
[13] T. Erneux, Applied Delay Differential Equations, Springer Science & Business Media, 2009.
[14] B.P. Mann, P.V. Bayly, M.A. Davies, J.E. Halley, Limit cycles, bifurcations, and accuracy of the milling process, J. Sound Vib. 277 (1–2) (2004) 31–48.
[15] X.H. Long, B. Balachandran, B. Mann, Dynamics of milling processes with variable time delays, Nonlinear Dynam. 47 (1) (2007) 49–63.
[16] X.H. Long, B. Balachandran, Stability analysis for milling process, Nonlinear Dynam. 49 (3) (2007) 349–359.
[17] M. Banihasan, F. Bakhtiari-Nejad, Chaotic vibrations in high-speed milling, Nonlinear Dynam. 66 (4) (2011) 557–574.
[18] Q. Yao, M. Luo, D. Zhang, B. Wu, Identification of cutting force coefficients in machining process considering cutter vibration, Mech. Syst. Signal Process. 103 (2018) 39–59.
[19] A.K. Kiss, D. Hajdu, D. Bachrathy, G. Stepan, Z. Dombovari, In-process impulse response of milling to identify stability properties by signal processing, J. Sound Vib. 527 (2022) 116849.
[20] Y. Altintas, E. Budak, Analytical prediction of stability lobes in milling, CIRP Ann. 44 (1) (1995) 357–362.
[21] M.A. Davies, J.R. Pratt, B. Dutterer, T.J. Burns, Stability prediction for low radial immersion milling, J. Manuf. Sci. Eng. 124 (2) (2002) 217–225.
[22] J. Tlusty, F. Ismail, Basic non-linearity in machining chatter, CIRP Ann. 30 (1) (1981) 299–304.
[23] Z. Li, Q. Liu, Solution and analysis of chatter stability for end milling in the time-domain, Chin. J. Aeronaut. 21 (2) (2008) 169–178.
[24] S.A. Jensen, Y.C. Shin, Stability analysis in face milling operations, Part 1: Theory of Stability Lobe prediction, J. Manuf. Sci. Eng. 121 (4) (1999) 600–605, http://dx.doi.org/10.1115/1.2833075.
[25] R. Szalai, G. Stépán, S.J. Hogan, Global dynamics of low immersion high-speed milling, Chaos 14 (4) (2004) 1069–1077.
[26] N.D. Sims, B. Mann, S. Huyanan, Analytical prediction of chatter stability for variable pitch and variable helix milling tools, J. Sound Vib. 317 (3–5) (2008) 664–686.
[27] Y. Altintas, M. Eynian, H. Onozuka, Identification of dynamic cutting force coefficients and chatter stability with process damping, CIRP Ann. 57 (1) (2008) 371–374.
[28] W. Chen, X. Teng, D. Huo, Q. Wang, An improved cutting force model for micro milling considering machining dynamics, Int. J. Adv. Manuf. Technol. 93 (9) (2017) 3005–3016.
[29] W. Chen, Z. Tong, D. Huo, W. Zhong, X. Jiang, A forward closed-loop virtual simulation system for milling process considering dynamics processing-machine interactions, Int. J. Adv. Manuf. Technol. 104 (5) (2019) 2317–2328.
[30] D. Montgomery, Y. Altintas, Mechanism of cutting force and surface generation in dynamic milling, J. Eng. Ind. 113 (2) (1991) 160–168, http://dx.doi.org/10.1115/1.2899673.
[31] M.L. Campomanes, Y. Altintas, An improved time domain simulation for dynamic milling at small radial immersions, J. Manuf. Sci. Eng. 125 (3) (2003) 416–422.
[32] T.L. Schmitz, J. Couey, E. Marsh, N. Mauntler, D. Hughes, Runout effects in milling: Surface finish, surface location error, and stability, Int. J. Mach. Tools Manuf. 47 (5) (2007) 841–851.
[33] M.B.G. Jun, X. Liu, R.E. DeVor, S.G. Kapoor, Investigation of the dynamics of microend milling - Part I: Model development, J. Manuf. Sci. Eng. 128 (4) (2006) 893–900, http://dx.doi.org/10.1115/1.2193546.
[34] K. Chen, H. Zhang, N. van de Wouw, E. Detournay, An alternative approach to compute chip thickness in milling, J. Manuf. Sci. Eng. 144 (11) (2022) http://dx.doi.org/10.1115/1.4054804.
[35] X. Liu, N. Vlajic, X. Long, G. Meng, B. Balachandran, Multiple regenerative effects in cutting process and nonlinear oscillations, Int. J. Dyn. Control 2 (1) (2014) 86–101.
[36] P. Wahi, A. Chatterjee, Self-interrupted regenerative metal cutting in turning, Int. J. Non-Linear Mech. 43 (2) (2008) 111–123.
[37] R.P.H. Faassen, N. van de Wouw, J.A.J. Oosterling, H. Nijmeijer, Prediction of regenerative chatter by modelling and analysis of high-speed milling, Int. J. Mach. Tools Manuf. 43 (14) (2003) 1437–1446.
[38] R.I. Leine, H. Nijmeijer, Dynamics and Bifurcations of Non-Smooth Mechanical Systems, Springer Science & Business Media, 2013.
[39] D. Bachrathy, G. Stepan, Improved prediction of stability lobes with extended multi frequency solution, CIRP Ann. 62 (1) (2013) 411–414.
[40] K.J. Bathe, Finite Element Procedures, Prentice Hall, 1996.
[41] D.S. Bale, R.J. Leveque, S. Mitran, J.A. Rossmanith, A wave propagation method for conservation laws and balance laws with spatially varying flux functions, SIAM J. Sci. Comput. 24 (3) (2003) 955–978.
[42] R.J. LeVeque, Finite Volume Methods for Hyperbolic Problems, Cambridge University Press, 2002.